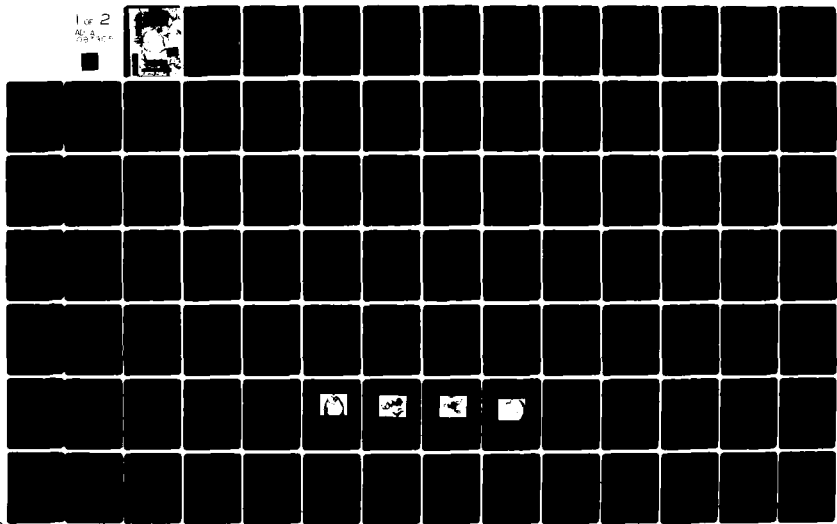


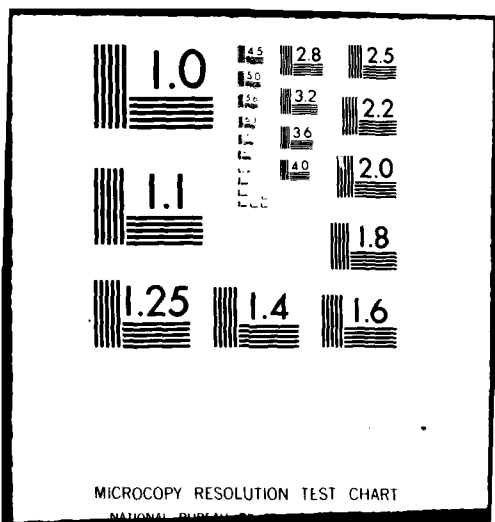
AD-A687 305

MASSACHUSETTS INST OF TECH CAMBRIDGE CORROSION LAB F/6 11/6
HYDROGEN INDUCED INTERGRANULAR CRACKING OF NICKEL-BASE ALLOYS. (U)
JUL 80 M KURKELA, T S LEE, R M LATANISION N00014-78-C-0002
NL

UNCLASSIFIED

1 of 2
M 1/2 300





LEVEL

ADA 087305

DDC FILE COPY
000

This document has been approved
for public release and sale; its
distribution is unlimited.

CORROSION LABORATORY
MASSACHUSETTS INSTITUTE OF TECHNOLOGY

(6) HYDROGEN INDUCED INTERGRANULAR
CRACKING OF NICKEL-BASE ALLOYS

by

(10) M./Kurkela & T.S.F./Lee
~~R.M.~~ /Latanision

(12) 207

(9) Technical Report No. 4

to

(14) TR-4

(15) Office of Naval Research
Contract No. N00014-78-C-0002, NR036-127/8-24-77(471)

(11) Jul 88

Reproduction in whole or in part is
permitted for any purpose of the
United States Government



✓ Corrosion Laboratory
Department of Materials Science and Engineering
Massachusetts Institute of Technology
Cambridge, Massachusetts 02139

July 1980

This document has been approved
for public release and sale; its
distribution is unlimited.

69.356 80 73 062

SECURITY CLASSIFICATION OF THIS PAGE (When Data Entered)

REPORT DOCUMENTATION PAGE		READ INSTRUCTIONS BEFORE COMPLETING FORM
1. REPORT NUMBER	2. GOVT ACCESSION NO.	3. RECIPIENT'S CATALOG NUMBER
		AD-A087 305
4. TITLE (and Subtitle) Hydrogen Induced Intergranular Cracking of Nickel-Base Alloys		5. TYPE OF REPORT & PERIOD COVERED Technical Report
		6. PERFORMING ORG. REPORT NUMBER
7. AUTHOR(s) M. Kurkela, T.S.F. Lee and R.M. Latanision		8. CONTRACT OR GRANT NUMBER(s) N00014-78-C-0002 ✓ NR036-127/8-24-77 (471)
9. PERFORMING ORGANIZATION NAME AND ADDRESS Massachusetts Institute of Technology Cambridge, Massachusetts 02139		10. PROGRAM ELEMENT, PROJECT, TASK AREA & WORK UNIT NUMBERS
11. CONTROLLING OFFICE NAME AND ADDRESS Office of Naval Research 800 Quincy Street Arlington, VA 22217		12. REPORT DATE July 1980
14. MONITORING AGENCY NAME & ADDRESS (if different from Controlling Office)		13. NUMBER OF PAGES 94
		15. SECURITY CLASS. (of this report)
		15a. DECLASSIFICATION/DOWNGRADING SCHEDULE
16. DISTRIBUTION STATEMENT (of this Report) This document is unclassified. Distribution and reproduction for any purpose of the US Government is permitted. This document has been approved for public release and sale; its distribution is unlimited.		
17. DISTRIBUTION STATEMENT (of the abstract entered in Block 20, if different from Report)		
18. SUPPLEMENTARY NOTES		
19. KEY WORDS (Continue on reverse side if necessary and identify by block number) hydrogen permeation, hydrogen embrittlement, nickel alloys, impurities		
20. ABSTRACT (Continue on reverse side if necessary and identify by block number) This report is intended to summarize the activities pursued during the second year of a program directed toward an evaluation of the susceptibility of nickel and nickel base alloys to embrittlement by cathodically produced hydrogen.		

BASIC DISTRIBUTION LIST

Technical and Summary Reports April 1978

<u>Organization</u>	<u>Copies</u>	<u>Organization</u>	<u>Copies</u>
Defense Documentation Center Cameron Station Alexandria, VA 22314	12	Naval Air Propulsion Test Center Trenton, NJ 08628 ATTN: Library	1
Office of Naval Research Department of the Navy 800 N. Quincy Street Arlington, VA 22217		Naval Construction Battalion Civil Engineering Laboratory Port Hueneme, CA 93043 ATTN: Materials Division	1
ATTN: Code 471 Code 102 Code 470	1 1 1	Naval Electronics Laboratory San Diego, CA 92152 ATTN: Electron Materials Sciences Division	1
Commanding Officer Office of Naval Research Branch Office Building 114, Section D 666 Summer Street Boston, MA 02210	1	Naval Missile Center Materials Consultant Code 3312-1 Point Mugu, CA 92041	1
Commanding Officer Office of Naval Research Branch Office 536 South Clark Street Chicago, IL 60605	1	Commanding Officer Naval Surface Weapons Center White Oak Laboratory Silver Spring, MD 20910 ATTN: Library	1
Office of Naval Research San Francisco Area Office One Hallidie Plaza Suite 601 San Francisco, CA 94102	1	David W. Taylor Naval Ship Research and Development Center Materials Department Annapolis, MD 21402	1
Naval Research Laboratory Washington, DC 20375		Naval Undersea Center San Diego, CA 92132 ATTN: Library	1
ATTN: Codes 6000 6100 6300 6400 2627	1 1 1 1 1	Naval Underwater System Center Newport, RI 02840 ATTN: Library	1
Naval Air Development Center Code 302 Warminster, PA 18964 ATTN: Mr. F. S. Williams	1	Naval Weapons Center China Lake, CA 93555 ATTN: Library	1
		Naval Postgraduate School Monterey, CA 93940 ATTN: Mechanical Engineering Department	1

BASIC DISTRIBUTION LIST (cont'd)

<u>Organization</u>	<u>Copies</u>	<u>Organization</u>	<u>Copies</u>
Naval Air Systems Command Washington, DC 20360 ATTN: Codes 52031 52032	1	NASA Headquarters Washington, DC 20546 ATTN: Code RRM	1
Naval Sea System Command Washington, DC 20362 ATTN: Code 035	1	NASA Lewis Research Center 21000 Brookpark Road Cleveland, OH 44135 ATTN: Library	1
Naval Facilities Engineering Command Alexandria, VA 22331 ATTN: Code 03	1	National Bureau of Standards Washington, DC 20234 ATTN: Metallurgy Division Inorganic Materials Div.	1
Scientific Advisor Commandant of the Marine Corps Washington, DC 20380 ATTN: Code AX	1	Director Applied Physics Laboratory University of Washington 1013 Northeast Fortheth Street Seattle, WA 98105	1
Naval Ship Engineering Center Department of the Navy Washington, DC 20360 ATTN: Code 6101	1	Defense Metals and Ceramics Information Center Battelle Memorial Institute 505 King Avenue Columbus, OH 43201	1
Army Research Office P.O. Box 12211 Triangle Park, NC 27709 ATTN: Metallurgy & Ceramics Program	1	Metals and Ceramics Division Oak Ridge National Laboratory P.O. Box X Oak Ridge, TN 37380	1
Army Materials and Mechanics Research Center Watertown, MA 02172 ATTN: Research Programs Office	1	Los Alamos Scientific Laboratory P.O. Box 1663 Los Alamos, NM 87544 ATTN: Report Librarian	1
Air Force Office of Scientific Research Bldg. 410 Boeing Air Force Base Washington, DC 20332 ATTN: Chemical Science Directorate Electronics & Solid State Sciences Directorate	1	Argonne National Laboratory Metallurgy Division P.O. Box 229 Lemont, IL 60439	1
Air Force Materials Laboratory Wright-Patterson AFB Dayton, OH 45433	1	Brookhaven National Laboratory Technical Information Division Upton, Long Island New York 11973 ATTN: Research Library	1
Library Building 50, Rm 134 Lawrence Radiation Laboratory Berkeley, CA	1	Office of Naval Research Branch Office 1030 East Green Street Pasadena, CA 91106	1

C
January 1979

SUPPLEMENTARY DISTRIBUTION LIST

Technical and Summary Reports

Dr. T. R. Beck
Electrochemical Technology Corporation
10035 31st Avenue, NE
Seattle, Washington 98125

Professor I. M. Bernstein
Carnegie-Mellon University
Schenley Park
Pittsburgh, Pennsylvania 15213

Professor H. K. Birnbaum
University of Illinois
Department of Metallurgy
Urbana, Illinois 61801

Dr. Otto Buck
Rockwell International
1049 Camino Dos Rios
P. O. Box 1085
Thousand Oaks, California 91360

Dr. David L. Davidson
Southwest Research Institute
8500 Culebra Road
P. O. Drawer 28510
San Antonio, Texas 78284

Dr. D. J. Duquette
Department of Metallurgical Engineering
Rensselaer Polytechnic Institute
Troy, New York 12181

Professor R. T. Foley
The American University
Department of Chemistry
Washington, D. C. 20016

Mr. G. A. Gehring
Ocean City Research Corporation
Tennessee Avenue & Beach Thorofare
Ocean City, New Jersey 08226

Dr. J. A. S. Green
Martin Marietta Corporation
1450 South Rolling Road
Baltimore, Maryland 21227

Professor R. H. Heidersbach
University of Rhode Island
Department of Ocean Engineering
Kingston, Rhode Island 02881

Professor H. Herman
State University of New York
Material Sciences Division
Stony Brook, New York 11970

Professor J. P. Hirth
Ohio State University
Metallurgical Engineering
1314 Kinnear Road
Columbus, Ohio 43212

Dr. E. W. Johnson
Westinghouse Electric Corporation
Research and Development Center
1310 Beulah Road
Pittsburgh, Pennsylvania 15235

Professor R. M. Latanision
Massachusetts Institute of Technology
77 Massachusetts Avenue
Room E19-702
Cambridge, Massachusetts 02139

Dr. F. Mansfeld
Rockwell International Science Center
1049 Camino Dos Rios
P. O. Box 1085
Thousand Oaks, California 91360

Dr. Jeff Perkins
Naval Postgraduate School
Monterey, California 93940

C
January 1979

SUPPLEMENTARY DISTRIBUTION LIST
(Continued)

Professor H. W. Pickering
Pennsylvania State University
Department of Material Sciences
University Park, Pennsylvania 16802

Dr. E. A. Starke, Jr.
Georgia Institute of Technology
School of Chemical Engineering
Atlanta, Georgia 30332

Dr. Barry C. Syrett
Stanford Research Institute
333 Ravenswood Avenue
Menlo Park, California 94025

Dr. R. P. Wei
Lehigh University
Institute for Fracture and
Solid Mechanics
Bethlehem, Pennsylvania 18015

Professor H. G. F. Wilsdorf
University of Virginia
Department of Materials Science
Charlottesville, Virginia 22903

Dr. Clive Clayton
State University of New York
Material Sciences Division
Stony Brook, New York 11970

Accession For	
NTIS GEN&I.	
DDC TAB	
Unannounced	
Justification <i>for 1/20/82</i>	
By <i>filed 10 Jul 80</i>	
Distribution/	
Availability Codes	
Dist	Avail and/or special

A

TABLE OF CONTENTS

	<u>Page</u>
LIST OF TABLES	iii
LIST OF FIGURES	iv
1. INTRODUCTION	1
2. BACKGROUND	2
2.1 Role of Impurity Segregation in Hydrogen- Induced Intergranular Cracking of Metals	2
2.2 The Role of Mobile Dislocation in the Transport of Hydrogen and Its Implications on Hydrogen- Induced Cracking	5
3. EXPERIMENTAL	7
3.1 Materials	7
3.2 Hydrogen Permeation Measurements	13
3.3 Straining Electrode Experiments	18
3.4 Cathodic Polarization Curves	24
3.5 Grain Boundary Open Circuit Measurements	25
4. RESULTS	26
4.1 Permeation Measurements in Unstrained Ni	26
4.2 Permeation Measurements on Nickel Undergoing Plastic Deformation	28
4.3 Straining Electrode Experiments	46
4.4 Cathodic Polarization Curves	65
4.5 Grain Boundary Electrode Measurements	70
5. DISCUSSION	73
5.1 Dislocation Transport of Hydrogen	73
5.2 Role of Impurities in Hydrogen Permeation	77

	<u>Page</u>
5.3 Discussion of Straining Electrode Experiments	82
5.4 The Effect of Promoters on Permeation of Hydrogen	86
5.5 Diffusion Kinetics Considerations	89
6. CONCLUSIONS	90
ACKNOWLEDGEMENTS	91
REFERENCES	92

LIST OF TABLES

	<u>Page</u>
TABLE I CHEMICAL COMPOSITIONS OF MATERIALS	8
TABLE II HEAT TREATMENT OF MATERIALS	11
TABLE III A SUMMARY OF HYDROGEN DIFFUSIVITY AND PERMEABILITY MEASUREMENTS IN MARZ Ni, Ni 270 and Ni 200	27
TABLE IV EFFECT OF GRAIN SIZE ON PERMEABILITY AND DIFFUSIVITY OF HYDROGEN	34
TABLE V HYDROGEN DIFFUSIVITY IN Ni 270 UNDERGOING PLASTIC DEFORMATION	40
TABLE VI EFFECT OF APPLIED POTENTIAL ON EMBRITTLE- MENT	48
TABLE VII EFFECT OF THERMAL TREATMENT ON EMBRITTLE- MENT	55
TABLE VIII EFFECT OF POISON ADDITION ON EMBRITTLEMENT	56
TABLE IX EFFECT OF POISON ADDITION ON EMBRITTLEMENT	57
TABLE X EFFECT OF STRAIN RATE ON EMBRITTLEMENT	59
TABLE XI OPEN CIRCUIT POTENTIALS OF GRAIN BOUNDARIES IN Ni 270 AS A FUNCTION OF HEAT TREATMENT	71
TABLE XII SIGNIFICANCE OF DISLOCATION TRANSPORT OF H	78

LIST OF FIGURES

	<u>Page</u>
FIGURE 1. The role of grain boundary segregation as an embrittling agent according to Latanision and Opperhauser [1].	4
FIGURE 2. The synergistic hydrogen embrittlement model of Yoshino and McMahon [15].	4
FIGURE 3. Grain boundary segregation of sulfur in Ni 200 as a function of temperature [27].	9
FIGURE 4. Typical microstructure of pure nickel (Ni 270 annealed condition). Grain size 450 μ m. Etchant 50% HNO ₃ + 50% CH ₃ COOH. Magnification 25x.	9
FIGURE 5. Tensile specimen for the straining electrode experiment.	12
FIGURE 6. Apparatus for hydrogen permeation studies.	14
FIGURE 7. Dimensions of tensile specimen used for hydrogen permeation studies in the presence of plastic deformation.	17
FIGURE 8. A typical hydrogen permeation transient in unstrained nickel.	19
FIGURE 9. Straining electrode experiment.	21
FIGURE 10. Electrode holder design for the straining electrode experiment.	22
FIGURE 11. Effect of thermal treatment on hydrogen permeability in Ni 200. a) I _C = 0.2mA/cm ² b) I _C = 0.8mA/cm ² .	29
FIGURE 12. Effect of thermal treatment on hydrogen permeability in Ni 270. a) I _C = 0.2mA/cm ² b) I _C = 0.8mA/cm ² .	30
FIGURE 13. Effect of thermal treatment on hydrogen permeability in Marz Ni. a) I _C = 0.2mA/cm ² b) I _C = 0.8mA/cm ² .	31
FIGURE 14. Effect of Na ₂ S on hydrogen permeability in Ni 270.	32
FIGURE 15. Effect of NaAsO ₂ on hydrogen permeability in Ni 200.	33

	<u>Page</u>
FIGURE 16. Effect of grain size on hydrogen permeability in Ni 270.	35
FIGURE 17. A schematic showing the steps involved in running a permeation experiment on a specimen undergoing plastic deformation.	36
FIGURE 18. Effect of strain rate on hydrogen permeability in Ni 270 undergoing plastic deformation.	39
FIGURE 19. Effect of strain rate on decay transient (recorded on switching off the charging current).	42
FIGURE 20. Effect of charging current on hydrogen permeability in Ni 270 undergoing plastic deformation.	44
FIGURE 21. Effect of promoter additions on hydrogen permeability on Ni 270 undergoing plastic deformation.	45
FIGURE 22. Effect of grain size on hydrogen permeability in Ni 270 undergoing plastic deformation.	47
FIGURE 23. Effect of thermal treatment on embrittlement; Ni 200, swaged 70%; annealed at 1200°C for 1 hr + 24 hr aging; grain size 300 μ m.	50
FIGURE 24. Effect of thermal treatment on embrittlement; Ni 200; swaged 70%; annealed at 1100°C for 1 hr + 24 hr aging; grain size 50 μ m.	52
FIGURE 25. Effect of thermal treatment on embrittlement; Ni 270; swaged 76%; annealed at 1100°C for 1 hr + 24 hr aging; grain size 200 μ m.	53
FIGURE 26a. Fracture surface of Ni 270 broken in air, 60x.	61
FIGURE 26b. Fracture surface of Ni 270 broken in deaerated 1N H ₂ SO ₄ at -600mV SCE, 60x.	62
FIGURE 26c. Fracture surface of Ni 200 broken in deaerated 1N H ₂ SO ₄ at -600mV SCE, 60x.	63
FIGURE 26d. Fracture surface of Ni 270 precharged at 10mA/cm ² for 165 hr and broken in air, 60x.	64
FIGURE 27. Effect of thermal treatment on cathodic polarization behavior of Ni 270 in 0.1N H ₂ SO ₄	66

	<u>Page</u>
FIGURE 28. Effect of thermal treatment on cathodic polarization behavior of Ni 200 in 0.1N H ₂ SO ₄ .	67
FIGURE 29. Effect of different poisons on cathodic polarization behavior in 0.1N H ₂ SO ₄ .	69
FIGURE 30. Effect of grain size and stacking fault energy on the hydrogen transport efficiency by the dislocation mode according to the model by Tien et al. [3].	75
FIGURE 31. Stress distribution and plastic zone ahead of a propagating crack according to Rice [38].	75
FIGURE 32. Evan's diagram [39].	80
FIGURE 33. Diagram showing schematically the effect of promoter elements on hydrogen evolution kinetics.	88

1. INTRODUCTION

In recent years, research on hydrogen-induced cracking of different metals and alloys (e.g., nickel base and iron base alloys) has brought to attention two aspects of the problem that have been widely discussed: the role of impurity segregation (segregation greatly increases hydrogen susceptibility) and the role of mobile dislocations in the transport of hydrogen (this provides for transport of hydrogen at rates much faster than lattice diffusion). A better understanding of these phenomena should contribute to development of more resistant alloys.

In this project, these two phenomena have been extensively investigated in pure Ni and are under study in some Ni-base alloys. The impurity segregation work has largely evolved from the earlier studies of Latanision and Opperhauser [1,2]. The approach involves use of hydrogen permeation experiments, straining electrode experiments at cathodic potentials, determination of cathodic polarization behavior and characterization of electrochemical properties (open circuit potential, polarization behavior) of grain boundaries. The dislocation transport study has been inspired mainly by the analytical work of Tien et al., [3] and involves the use of the hydrogen permeation technique on specimens undergoing plastic deformation.

2. BACKGROUND

2.1 Role of Impurity Segregation in Hydrogen-Induced Intergranular Cracking of Metals

Several recent studies have shown that the susceptibility of many metals and alloys to intergranular hydrogen-induced cracking is greatly increased as a result of grain boundary segregation of certain impurities. These impurities are metalloids such as S, P, Sn and Sb which are known to enhance absorption of hydrogen when added to the electrolyte in small amounts, i.e., which are promoters or hydrogen recombination positions. Berkowitz and Kane [4,5] have shown an association between hydrogen cracking susceptibility and segregation of P in Hastelloy C276 and a similar effect in MP35N due to segregation of S and P. Frandsen et al., [6] have shown a similar association in Ni-Co alloys due to segregation of S. Grain boundary segregation of S is known to embrittle pure Ni, also [7]. Hydrogen susceptibility is greatest in steels tempered in the temperature range for maximum temper embrittlement [15]. Temper embrittlement is known to be associated with grain boundary segregation of P, Sb and Sn as well as Ni and Cr [8,9]. Also, other examples can be found in the literature [10].

One can look at the effects of grain boundary segregation from a chemical/electrochemical point of view and a mechanical point of view. The difference in composition between the grain interior and the segregated grain boundary may cause electrochemical and chemical differences, such as [11,12]:

- the electrode potentials of the matrix and grain boundary differ from each other
- the anodic and cathodic polarization behavior of the grain boundary and matrix may be different
- the solubility of hydrogen in the grain boundary differs from the solubility in the matrix
- segregation may affect kinetics of hydrogen diffusion

From a mechanical point of view, grain boundary segregation can cause effects such as [13,]4]:

- a lowering of grain boundary surface energy and thus facilitation of crack propagation
- the mechanical properties of grain boundaries can be different from those of the matrix, e.g., grain boundary hardness often increases as a result of segregation
- segregation may affect dislocation processes occurring at the grain boundary.

Two principal models have been proposed to explain the deleterious effect of segregation. Latanision and Opperhauser [1] suggest that the segregated impurities act by promoting the absorption of hydrogen in the proximity of grain boundaries. Subsequently, hydrogen is transported into the interior by dislocation transport and/or grain boundary diffusion [1,2]. The presence of hydrogen at the grain boundaries and the attendant stress concentration there then leads to cracking. This mechanism is illustrated in Figure 1. Yoshino and McMahon [15] propose that grain boundary segregation and hydrogen act cooperatively, resulting in embrittlement. According to the authors, grain

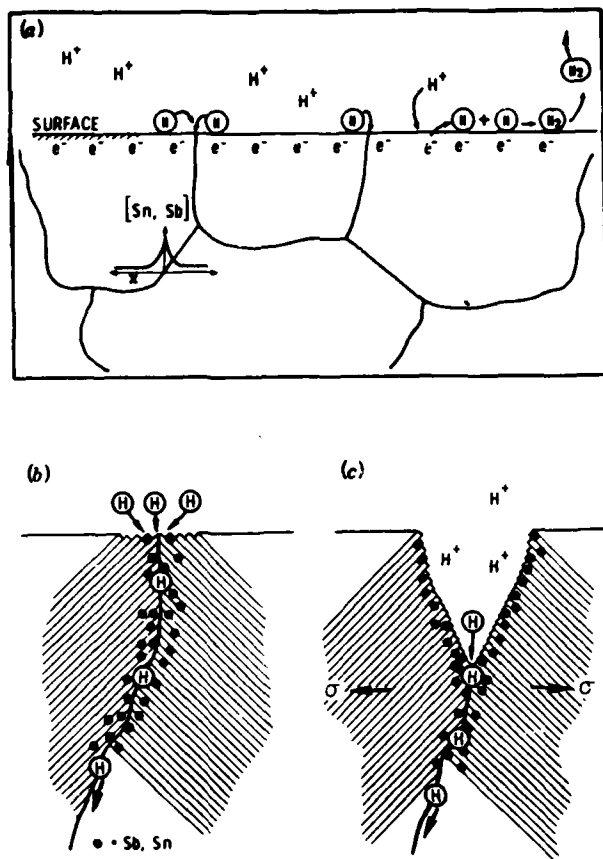


FIGURE 1. The role of grain boundary segregation as an embrittling agent according to Latanision and Opperhauser [1].

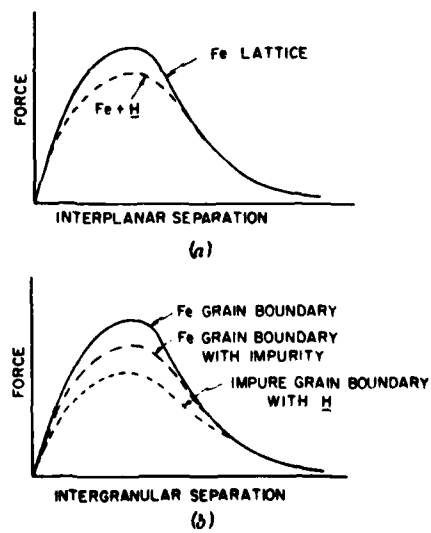


FIGURE 2. The synergistic hydrogen embrittlement model of Yoshino and McMahon [15].

boundary segregation lowers the decohesive force between grains and the presence of hydrogen lowers it even further. This mechanism is shown in Figure 2.

2.2 The Role of Mobile Dislocation in the Transport of Hydrogen and its Implications on Hydrogen-Induced Cracking

Bastien and Azou [16,17] were the first to suggest that hydrogen could be transported along with mobile dislocations. Later, the idea received additional support from observations of serrated yielding, tritium release measurements and autoradiographic techniques [18-24]. Recently, Tien et al [3] have proposed a quantitative model for this process and Hirth and Johnson [25] have developed a model for the kinetic supersaturations of hydrogen generated by dislocation transport.

A dislocation transport mode is important for the following reasons, as presented by Tien et al. [3]:

- a transport mode more rapid than lattice diffusion is essential in rationalizing experimentally observed fatigue crack growth rates in the presence of hydrogen
- transport of hydrogen along with mobile dislocation can account for hydrogen participation in SCC processes, when cracking rates exceed lattice diffusion rates
- it can explain alterations in the ductile fracture process caused by hydrogen

•it can explain hydrogen effects in a high pressure hydrogen test

Among results rationalized by dislocation transport, one can mention correlations between hydrogen compatibility and stacking fault energy, the effect of dispersed phases on hydrogen compatibility, sweeping of hydrogen to grain boundaries, environmental effects on fatigue crack growth and hydrogen participation in ductile rupture processes [3]. Although there is agreement that a dislocation mode may operate, whether dislocation transport is necessary for embrittlement or not is arguable. West and Louthan, for example, think that hydrogen effects in high pressure H₂ can be explained without dislocation transport [26].

3. EXPERIMENTAL

3.1 Materials

The materials employed for permeation studies and electrochemical evaluation were three grades of pure nickel, each having different impurity contents: Marz Ni (99.995% Ni), Ni 270 (99.97% Ni) and Ni 200 (99.5% Ni). The chemical compositions of these materials are shown in Table I.

Marz Ni is a very pure zone refined Ni grade. It was obtained from Materials Research Corporation in the form of cold-rolled strip, width 2.5cm and thickness 0.125mm. Ni 270 and Ni 200 were obtained through the courtesy of International Nickel Company. These materials were in the form of hot rolled plate, thickness 0.3cm. Strips were cut from these plates and cold rolled to a thickness of 0.45mm.

All the materials were recrystallized by annealing at 1000°C under an argon atmosphere and quenched in water. To investigate the effect of grain boundary segregation, part of the samples were subsequently heat treated at 650°C for 24 hr. The purpose of this treatment was to segregate sulfur to grain boundaries. Sulfur is the dominant segregating element in nickel [27,28]. Figure 3 shows the grain boundary segregation of S in Ni 200 as a function of temperature. Segregation takes place in the temperature range 300-700°C, with the maximum segregation occurring at about 600°C. According to these data by Smialowska et al. [27], a 12 hr treatment at 600°C results in a grain boundary sulfur

TABLE I
CHEMICAL COMPOSITIONS OF MATERIALS

<u>NICKEL</u>						
Chemical Analysis (wt%)						
	Ni	Fe	S	C	Cu	Si
Marz Ni	Major	0.002	0.000025	0.0015	-----	0.0017
Ni 270	Major	0.005	0.001	0.02	0.001	0.001
Ni 200	Major	0.15	0.005	0.1	0.1	0.05

TD nickel: 2 volume percent ThO₂ in a 99.92% Ni matrix

<u>NICKEL ALLOYS</u>						
Chemical Analysis (wt%)						
	Ni	Cr	Fe	C	Mn	S
Inconel 600	Balance	14-17	6-10	0.15	1.00	0.015
Incoloy 800	30-35	19-23	Balance	0.10	1.50	0.015

Ni	Si	Cu
Inconel 600	0.5	0.5
Incoloy 800	1.0	0.75

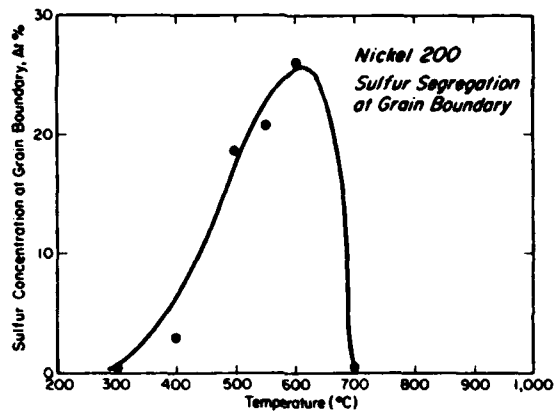


FIGURE 3. Grain boundary segregation of sulfur in Ni 200 as a function of temperature [27].

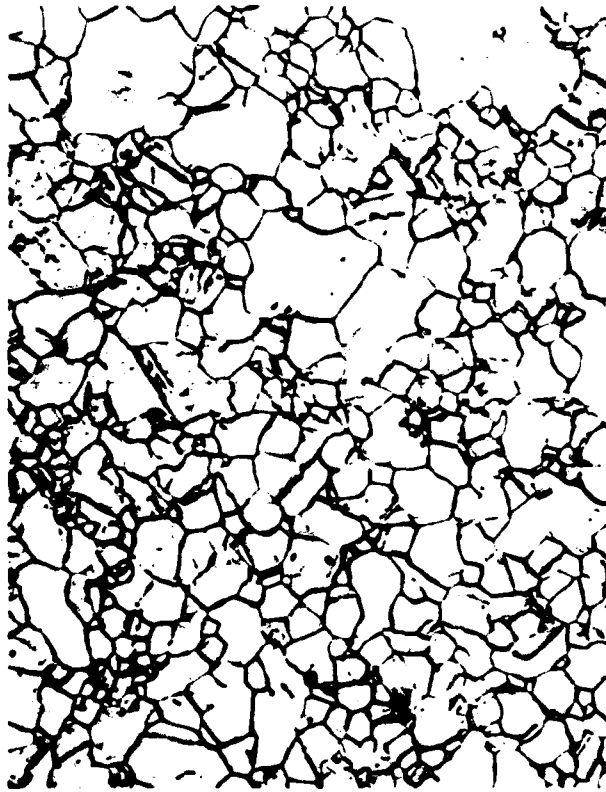


FIGURE 4. Typical microstructure of pure nickel (Ni 270, annealed condition). Grain size 450 μ m. Etchant 50% HNO₃ + 50% CH₃ COOH. Magnification 25x.

concentration of 25 atomic per cent. Probably, Ni 270 and Marz Ni behave similarly except that the impurity content is different. The heat treatments are summarized in Table II.

A typical microstructure of pure Ni (Ni 270) is shown in Figure 4. The recrystallization was carried out at 1000°C for 30 minutes to develop large grains. In this way, higher concentrations of S are likely to be attained at grain boundaries because in a large grain size material there is less grain boundary surface area per unit volume. The grain size of Ni 270 and Marz Ni was about 450 μm , that of the more impure Ni 200 about 150 μm . The materials were homogeneous and single phase; optical microscopy did not reveal any second phases. The 24 hr treatment at 650°C did not result in any additional grain growth.

The materials tested in the straining electrode experiments were mainly Nickel 270 and Nickel 200. Some preliminary work has been done on Inconel 600, the chemical composition of which is also listed in Table I. The materials as-received were in the form of 1/2 or 3/8 inch diameter cylindrical rods. First, these rods were cold-worked by swaging: Nickel 270 swaged down to 76% reduction in area, Nickel 200 swaged 70%, and Inconel 600 swaged 85%. These cold-worked rods were then cut and lathe-machined into tensile specimens whose dimensions are shown in Figure 5. Subsequently these tensile specimens were given various thermal treatments, as summarized in Table II. The Ni 270 specimens were solution-annealed at 1100°C for

TABLE II
HEAT TREATMENT OF MATERIALS

HEAT TREATMENTS FOR PERMEATION STUDIES
AND ELECTROCHEMICAL EVALUATION

Marz Ni Ann

Marz Ni Ann + 24h 650°C

Ni 270 Ann

Ni 270 Ann + 24h 650°C

Ni 200 Ann

Ni 200 Ann + 24h 650°C

HEAT TREATMENTS FOR STRAINING ELECTRODE EXPERIMENTS

Ni 270 Ann

Ni 270 Ann + 24h 400°C to 800°C

Ni 200 Ann

Ni 200 Ann + 24h 400°C to 800°C

Inconel 600 Ann

Inconel 600 Ann + 14h 700°C

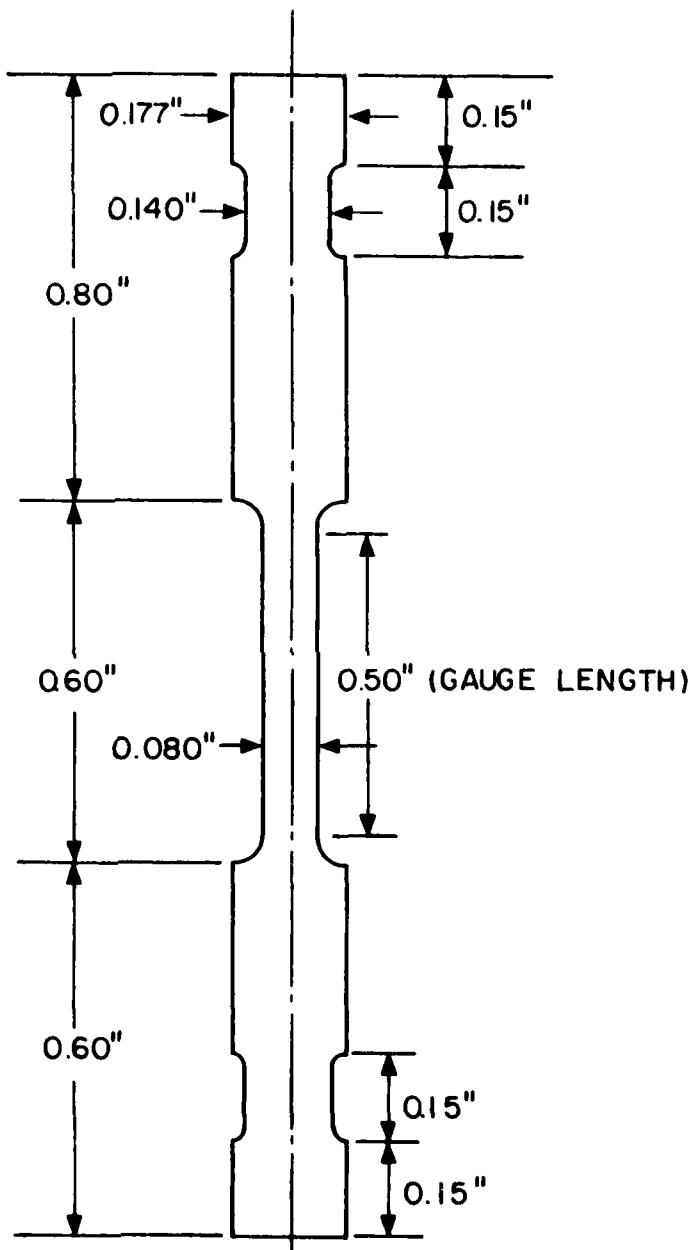
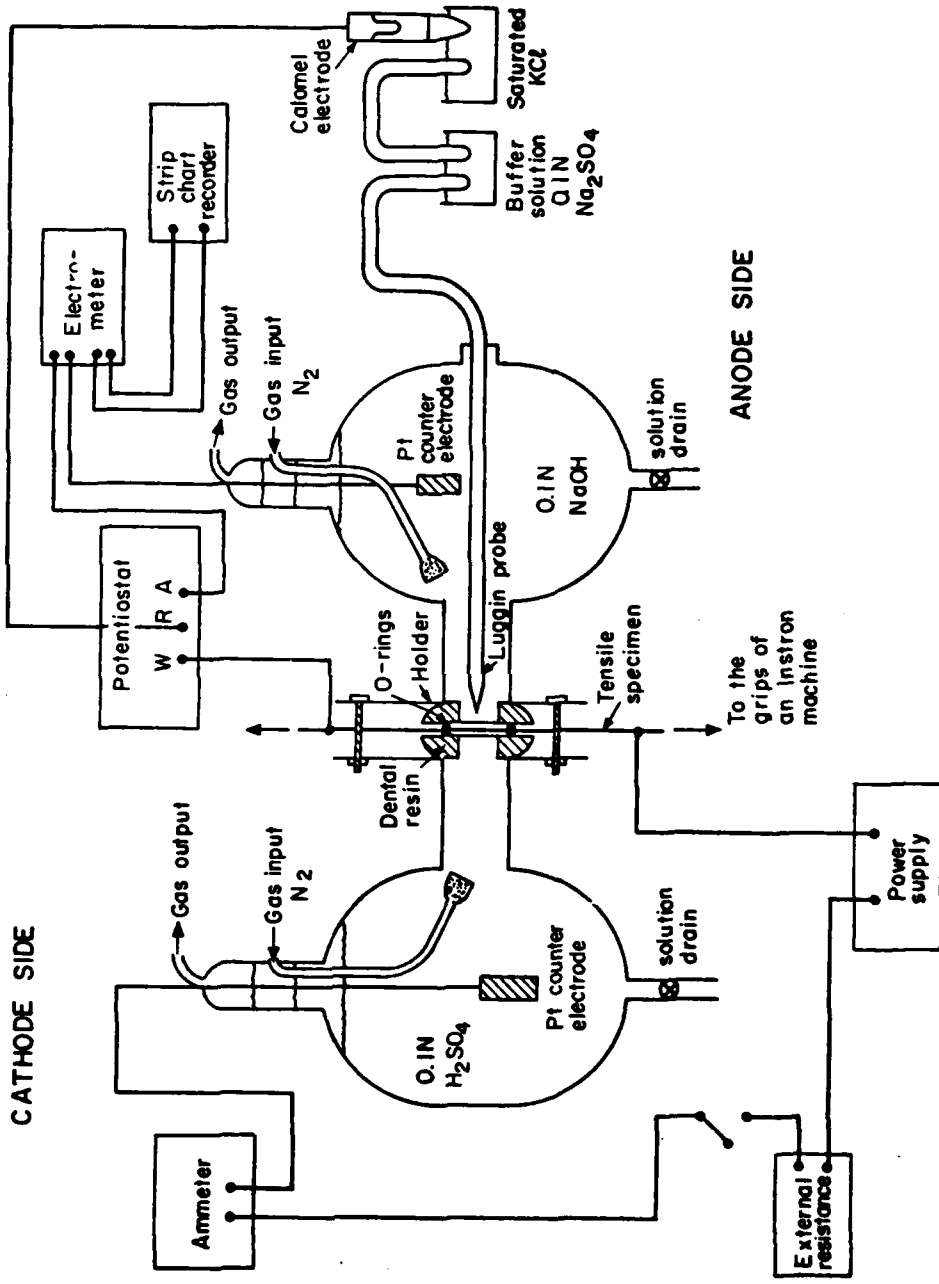


FIGURE 5. Tensile Specimen for the Straining Electrode Experiment

1 hour and the grain size attained was about 200μ , as determined by the line-intercept method. The more impure Nickel 200 was either annealed at 1100°C for 1 hour to yield a grain size of 50μ , or annealed at 1200°C for 1 hour giving a grain size of 300 microns. The Inconel 600 nickel-base alloy was annealed at 1200°C for 1 hour and the grain size was 300μ . Additional aging treatments were done on some Nickel 270 and Nickel 200 specimens at temperatures ranging from 400°C to 800°C for 24 hours. A single aging treatment at 700°C for 14 hours was also given to some Inconel 600 specimens. The purpose of these subsequent aging treatments was to promote impurity segregation at grain boundaries (see Figure 3, for example), and they did not alter the original grain sizes attained by annealing. In all thermal treatments, the specimens were encapsulated in quartz tubes filled with low pressure pure argon, and the specimens were quenched in water after each treatment.

3.2 Hydrogen Permeation Measurements

Hydrogen permeability in the materials and its dependence on various parameters was studied by means of the electrochemical permeation technique developed by Devanathan and Stachurski [29]. Figure 6 shows a schematic of the experimental apparatus. In this technique, the material under study is made a bielectrode and clamped between the cathodic (hydrogen entry) and anodic (hydrogen exit) compartments. The dimensions of the specimens were about



HYDROGEN PERMEATION CELL

FIGURE 6. Apparatus for hydrogen permeation studies.

3.0 x 3.0cm, the thickness varying in the range 65-90 μ m. A circular area of 1.27 cm² was exposed to the solution on each side. The electrolyte in the cathodic half-cell was 0.1N H₂SO₄, whereas 0.1N NaOH was used in the anodic compartment. Both solutions were deaerated with prepurified nitrogen both prior to the run and continuously during it to minimize the effects of oxygen.

Hydrogen is charged into the specimen by polarizing the cathodic side galvanostatically using the circuitry shown on the left in Figure 6. Part of the hydrogen produced thereby is absorbed and diffuses through the specimen to the anodic side. The anodic side is maintained at a constant potential of +100mV SCE (i.e., above the reversible potential for the hydrogen reaction) with the potentiostat so that the concentration of hydrogen on this surface is zero. When the hydrogen arrives on this side after diffusing through the specimen, it is immediately oxidized. This oxidation current can be measured and is directly proportional to the permeation rate of hydrogen. This current was measured with an electrometer and recorded with a strip chart recorder. All experiments were carried out at room temperature.

The specimens for the permeation studies were prepared by electropolishing in a 60% H₂SO₄ - 40% H₂O solution. A platinum electrode was used as the cathode and a current density of 300 mA/cm² was employed. The solution was stirred by a magnetic stirring bar during the process. For permeation studies, the anodic side was electrolessly plated with a thin layer of palladium using a

Pallamerse solution. The purpose of coating with Pd was to reduce the corrosion rate of the anodic side so that the oxidation of hydrogen would be the sole reaction. Coating with Pd does not have any effect on the permeation as can be shown by using the analysis of Kumnick and Johnson [30]. A thin Nichrome wire was spotwelded to the specimen for electrical contact. Before the experiment, the specimens were cleaned ultrasonically in acetone, rinsed in methanol and distilled water, and finally dried with hot air.

To study hydrogen permeation in specimens undergoing plastic deformation, the same technique was used. In this case, a thin tensile specimen served as the permeation membrane as well. The dimensions of the tensile specimen are shown in Figure 7. The gage length was 5cm and the reduced section width 1.9cm. The thickness was 0.43mm. The area exposed to solution was 0.32cm^2 . The specimen was mounted between the two compartments and the specimen-cell assembly was positioned between the cross-heads of an Instron machine. The anodic and cathodic half-cells were filled with the respective solutions. The specimens were deformed at a constant extension rate, with care taken to insure that no leaks occurred. After a constant background current is established, hydrogen charging is begun. Permeation currents are measured as described earlier.

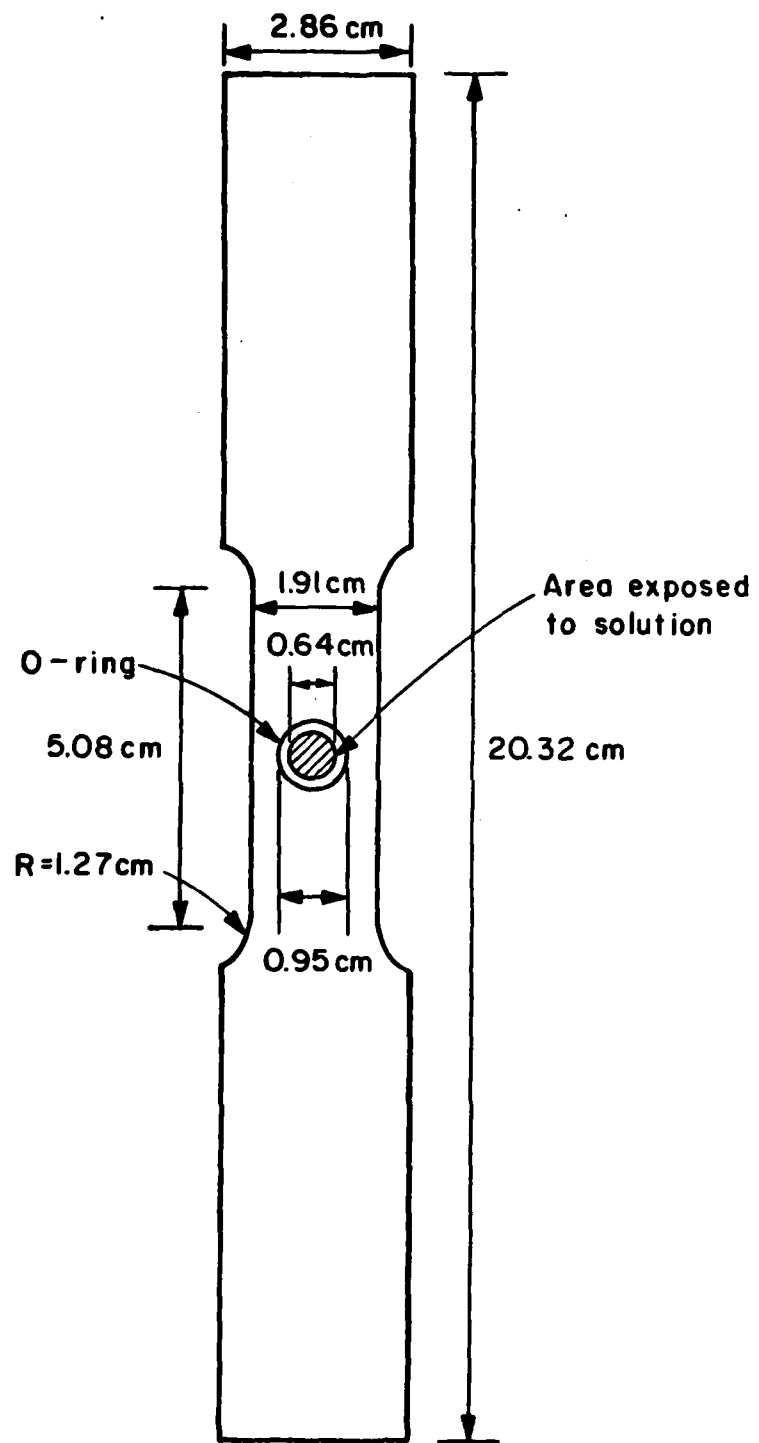


FIGURE 7. Dimensions of tensile specimen used for hydrogen permeation studies in the presence of plastic deformation.

A typical permeation transient in unstrained nickel is shown in Figure 8. First, the current remains at a low background value ($<0.1 \mu\text{A}/\text{cm}^2$). Once hydrogen arrives on the anodic side, the current starts to increase and finally reaches a steady state value. The mathematics of hydrogen permeation has been dealt with extensively in the literature [31-34]. By applying Fick's first and second laws with the appropriate initial and boundary conditions and solving this differential equation, one can evaluate the diffusion coefficient of hydrogen, D_H . Using the so-called time lag method one obtains for D_H the following expression [34].

$$D = L^2 / 2t_L \quad (1)$$

where L is the thickness of the specimen and t_L is the so-called time lag (= time required for the permeation current to reach 63% of the steady state value). Permeability, $J_\infty (\mu\text{A}, \text{cm}^2)$, and the diffusion coefficient of hydrogen, D_H , were measured in order to determine whether there are any correlations between hydrogen susceptibility and permeability and diffusivity.

3.3 Straining Electrode Experiments

The apparatus used in the straining electrode experiments

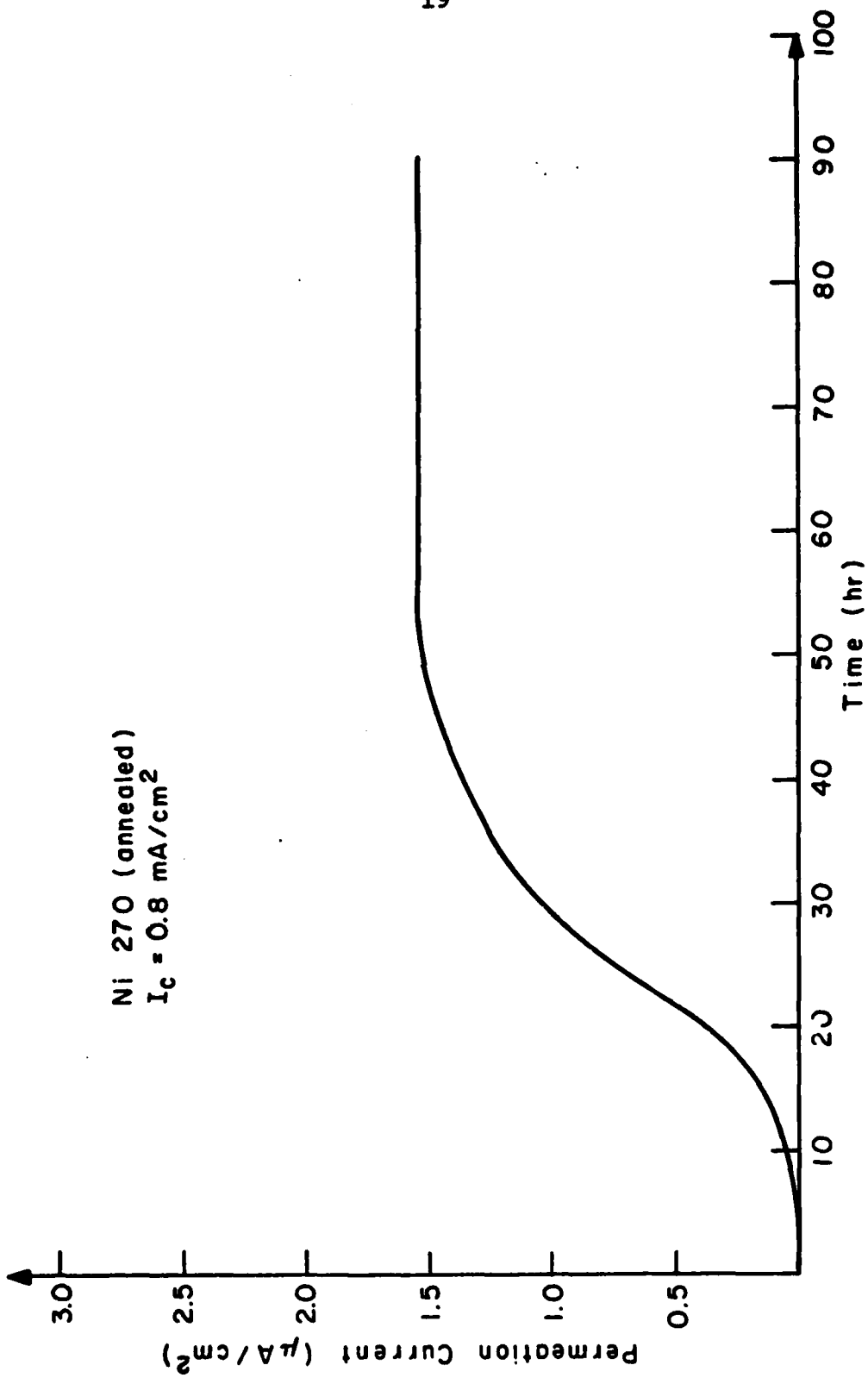


FIGURE 8. A typical hydrogen permeation transient in unstrained nickel.

consists of the modified standard polarization cell (made of pyrex) designed by Greene [35], as shown in Figure 9. In order to be able to apply a uniaxial tensile stress to the tensile specimen (Figure 5) which was positioned at the center of a cell, a bottom neck had been added to the cell. Two pairs of small split grips were used to grasp both ends of the specimen, and each pair was threaded to a cylindrical rod which was extended to the outside of the cell and was connected to the load cell of an Instron tension machine. This split grip design, Figure 10, was used to ensure secure grasp of the tensile specimen during straining. The whole electrode holder system (split grips and extension rods) was made of a hardened carbon steel. A teflon insulation system was machined to proper dimensions in order to insulate the electrode holders from the electrolyte in the cell and to keep the specimen/specimen-holder assembly in an up-right configuration. Two platinum counter electrodes were placed inside the cell through necks on top of the cell. The electrolyte was purged by bubbling pre-purified nitrogen gas through the fritted glass of a gas inlet-outlet pyrex tube to eliminate oxygen from the electrolyte. A pyrex Luggin probe was placed in the electrolyte so that the potential of the working electrode (i.e., the specimen) could be measured. The Luggin probe was filled with the same electrolyte as that which was used in the cell, and was connected to an external beaker filled with the same electrolyte. The beaker was

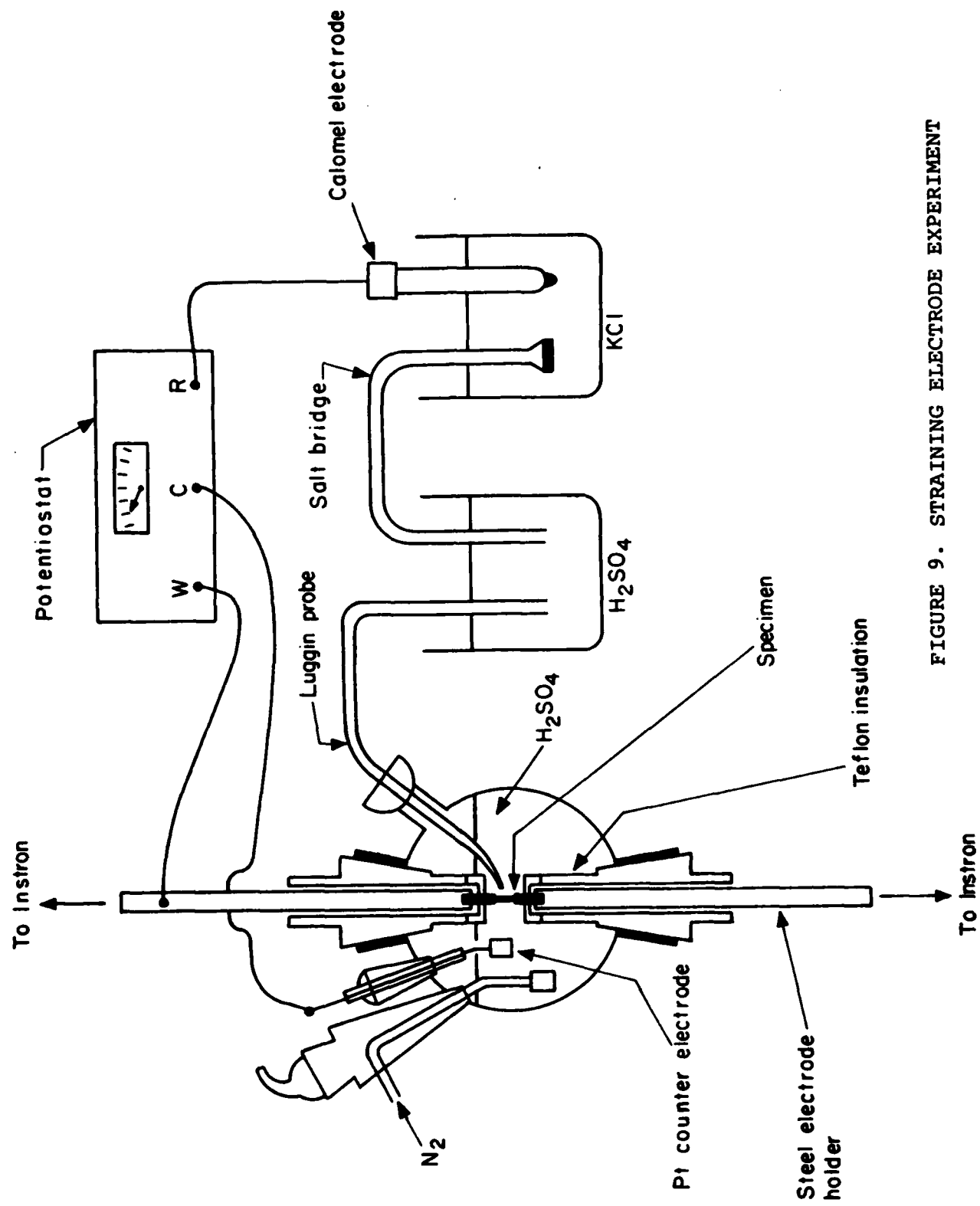


FIGURE 9. STRAINING ELECTRODE EXPERIMENT

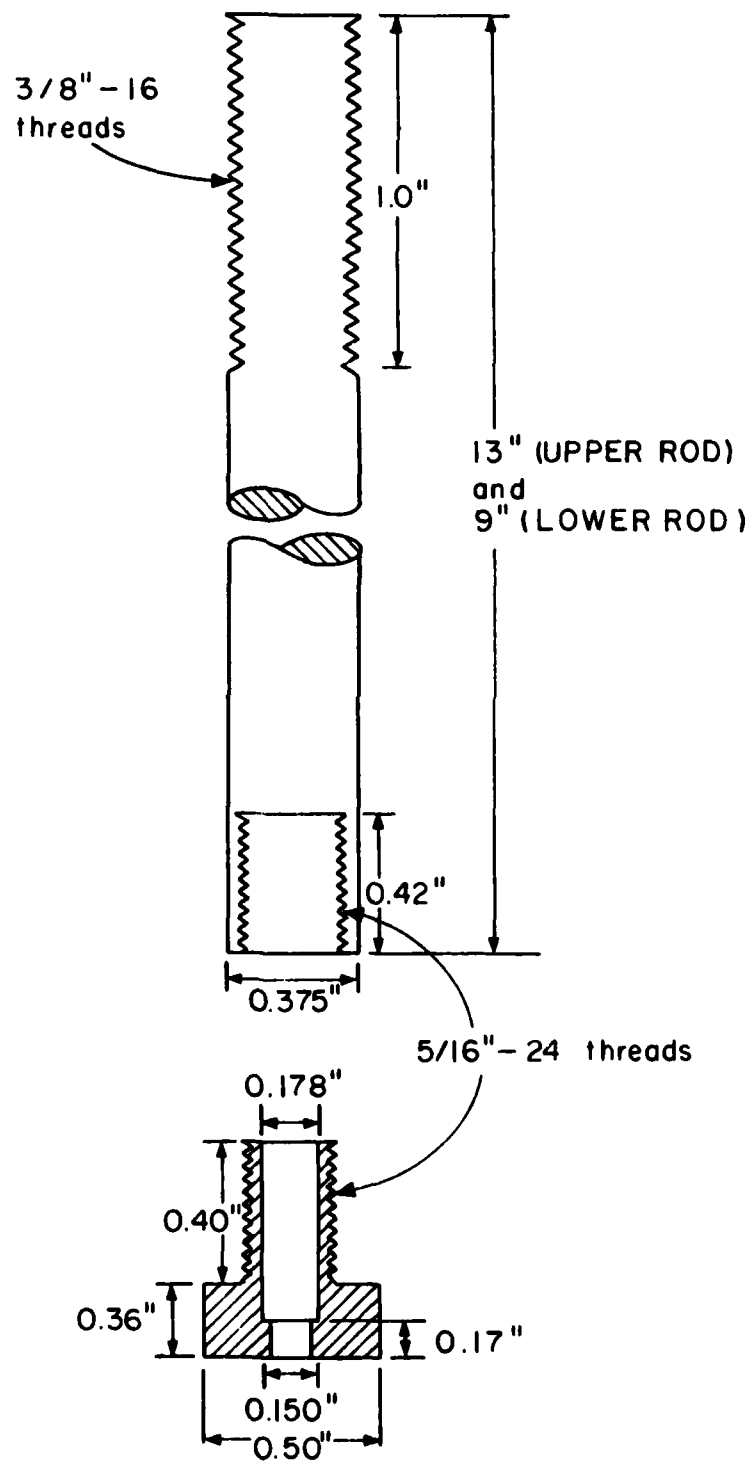


FIGURE 10. Electrode holder design for the straining electrode equipment.

in turn connected through a salt bridge to another beaker filled with KCl solution in which a saturated calomel reference electrode was half-immersed. With this arrangement, the chloride ions from the calomel electrode could be kept away from the working electrolyte, and the calomel electrode could be protected from being damaged by the working electrolyte. The liquid junction potentials in this circuit were negligibly small. The working, counter and reference electrodes were electrically linked to corresponding terminals of a Wenking potentiostat.

In the normal experimental procedure, the gauge section of the tensile specimen was first hand-polished with a 600 grade SiC paper. The thick sections of the specimen were covered with a microstop lacquer so that only the gauge section would be exposed to the electrolyte. The gauge length and diameter were measured. The specimen was then ultrasonically cleaned in methanol. After this specimen preparation, the arrangement shown in Figure 9 was set up. The working electrolyte had been deaerated for at least 1 hour and the deaeration was continued during the experiment. The specimen was simultaneously strained and polarized potentiostatically at a selected potential. During the test, the load vs displacement curve was plotted automatically in the Instron and the polarizing current was monitored by a strip-chart recorder connected to the potentiostat. After fracture, the plastic fracture elongation was determined from the load curve, and the fracture surface was examined under an optical stereo microscope and/or a scanning electron microscope.

Except for the high strain-rate experiments, all experiments were run at an initial strain rate of about $6 \times 10^{-5} \text{ s}^{-1}$. Most experiments were run at a cathodic potential of -600mV SCE with a corresponding cathodic current around 3mA/cm^2 . The electrolyte used was exclusively deaerated 1N H_2SO_4 . All experiments were done at room temperature under normal laboratory atmosphere.

3.4 Cathodic Polarization Curves

To characterize the hydrogen evolution on the surfaces of the different materials, cathodic polarization curves were determined for Marz Ni, Ni 270 and Ni 200 both in the annealed and annealed + heat treated conditions. The specimens were polished with grinding papers up to 500 grade. A Nichrome wire was spot-welded to the specimen for electrical contact. The specimens were cleaned ultrasonically in acetone. Microstop lacquer was used to mask off a circular 2.5cm^2 area for polarization studies. Just before the run, the surface of the specimen was gently rubbed with 500 emery paper, the specimen was cleaned in methanol, rinsed in distilled water and dried with hot air.

A standard double compartment polarization cell was used. The 0.1N H_2SO_4 solution was deaerated with prepurified nitrogen for 24 hours prior to the experiment and deaeration was continued during the experiment. Galvanostatic polarization curves were determined. A platinum counter electrode and a saturated calomel reference electrode were used.

Also, the effect of promoter elements on cathodic polarization behavior was studied. For this purpose, small amounts of NaAsO_2 , Sb_2O_3 , Na_2S and Na_2SeO_3 were added to the 0.1N H_2SO_4 solution.

3.5 Grain Boundary Open Circuit Potential Measurements

Because it is possible that grain boundary segregation affects the electrode potential of the grain boundary, the effect of thermal treatment in the segregation range was studied by aging Ni 270 samples at 400-800°C. Notched specimens of Ni 270 were machined. The specimens were annealed at 1100°C for 30 minutes, after which 24 hr aging treatments were carried out at 400, 500, 600, 700 and 800°C. Next, the specimens were charged with hydrogen in a 5% H_2SO_4 + 5mg/l NaAsO_2 solution for 250 hr using a charging current of 100 mA/cm². After charging, the specimens were fractured in an Instron machine. The fracture is 100% intergranular. Immediately after fracture, the specimen is painted with lacquer except for the fracture surface and transferred quickly to a polarization cell for open circuit potential determination. The time from fracture to open circuit potential measurement was less than 10 min so that the surface was a relatively "fresh" fracture surface. Since the fracture is completely intergranular, the open circuit potential of the fracture surface is that of the grain boundary.

4. RESULTS

4.1 Permeation Measurements in Unstrained Ni

4.1.1 The effect of thermal treatment

The results of hydrogen permeation measurements in both the annealed and annealed + aged (24 hr 650°C) conditions are summarized in Table III. Permeabilities and diffusivities for segregated and unsegregated specimens were determined for two different charging currents: 0.2 mA/cm^2 ($= -470\text{mV SCE}$) and 0.8 mA/cm^2 ($= -580\text{mV SCE}$). At -470mV SCE anodic processes are still thermodynamically possible, at -580mV SCE they are not.

Three observations can be made:

- thermal treatment at 650°C increases permeability at a charging current of 0.2 mA/cm^2 . In Marz Ni the effect is very small, but in the more impure Ni 270 and Ni 200 the effect is more pronounced. Thus, the higher the bulk S content the higher the increase in permeability, J_∞ .
- at a charging current of 0.8 mA/cm^2 , the thermal treatment has no effect on permeability in either Ni 270 or Ni 200
- the diffusion coefficient of hydrogen decreases in the order $D_{\text{Marz Ni}} > D_{\text{Ni 270}} > D_{\text{Ni 200}}$; i.e., with higher alloying and impurity content. In Marz Ni, the diffusion coefficient of H is not affected by heat treatment and charging current. In Ni 270 and Ni 200, there is the following trend: the higher the permeability, the higher the diffusion coefficient.

TABLE III
A SUMMARY OF HYDROGEN DIFFUSIVITY AND PERMEABILITY MEASUREMENTS
in MARZ Ni, Ni 270 AND Ni 200

Material and Treatment	I_C ($\mu\text{A}/\text{cm}^2$)	D (cm^2/s)	J_∞ ($\mu\text{A}/\text{cm}^2$)
MARZ Ni Ann	0.2	5.4×10^{-10}	0.11
MARZ Ni Ann + 24h 650°C	0.2	5.4×10^{-10}	0.28
MARZ Ni Ann	0.8	5.6×10^{-10}	0.50
Ni 270 Ann	0.2	2.5×10^{-10}	0.38
Ni 270 Ann + 24h 650°C	0.2	3.4×10^{-10}	1.44
Ni 270 Ann	0.8	3.3×10^{-10}	1.54
Ni 270 Ann + 24h 650°C	0.8	3.3×10^{-10}	1.72
Ni 200 Ann	0.2	1.7×10^{-10}	0.68
Ni 200 Ann + 24h 650°C	0.2	2.7×10^{-10}	3.23
Ni 200 Ann	0.8	2.1×10^{-10}	1.39
Ni 200 Ann + 24h 650°C	0.8	2.1×10^{-10}	1.18

The effect of thermal treatment at 650°C for the two charging currents is shown in Figures 11-13.

4.1.2 Effect of promoters

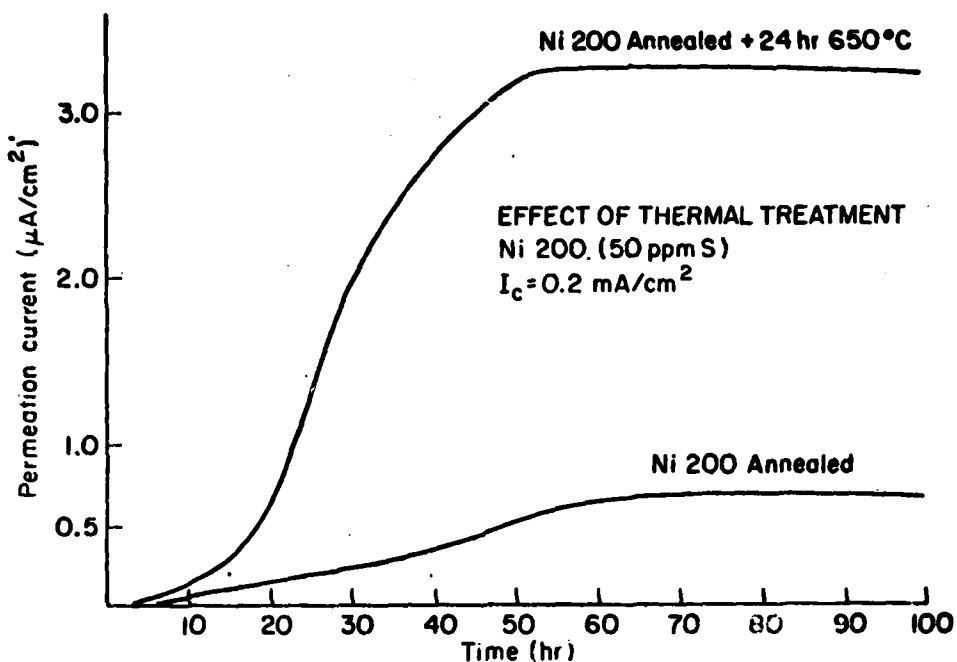
The effect of promoter elements, usually group V-A and VI-A elements such as As, Sb, P (V-A), S, Se, Te (VI-A), was also studied. As was selected from group V-A and S from group VI-A. In one case 1.5mg/l NaAsO₂ was added and in the other 15mg/l Na₂S was added. In both cases, permeability was increased significantly. The results are shown in Figures 14 and 15.

4.1.3 Effect of grain size

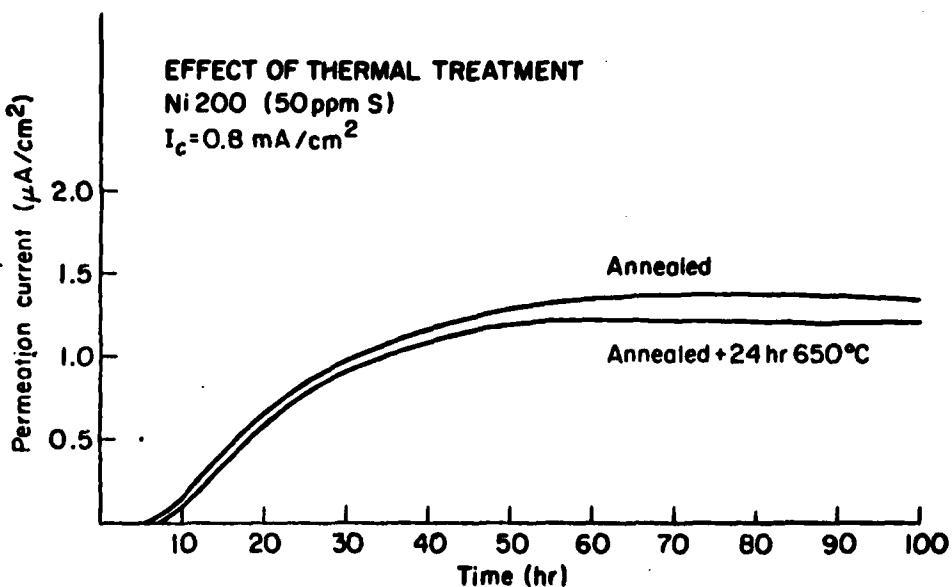
The grain size of the material should play a role in hydrogen permeability if there is any short circuit grain boundary diffusion. In such a case, diffusivity and permeability should be functions of grain size. To study this, permeation experiments were performed on two Ni 270 specimens. Both were solution annealed at 1000°C, but one for a short time (3 min) which resulted in grain size of 50µm and the other for a long time (45 min) which resulted in a grain size of 750µm. A charging current of 0.8 mA/cm² was used. The results are shown in Table IV and the transients in Figure 16.

4.2 Permeation Measurements on Nickel Undergoing Plastic Deformation

Figure 17 describes the steps involved in running a permeation

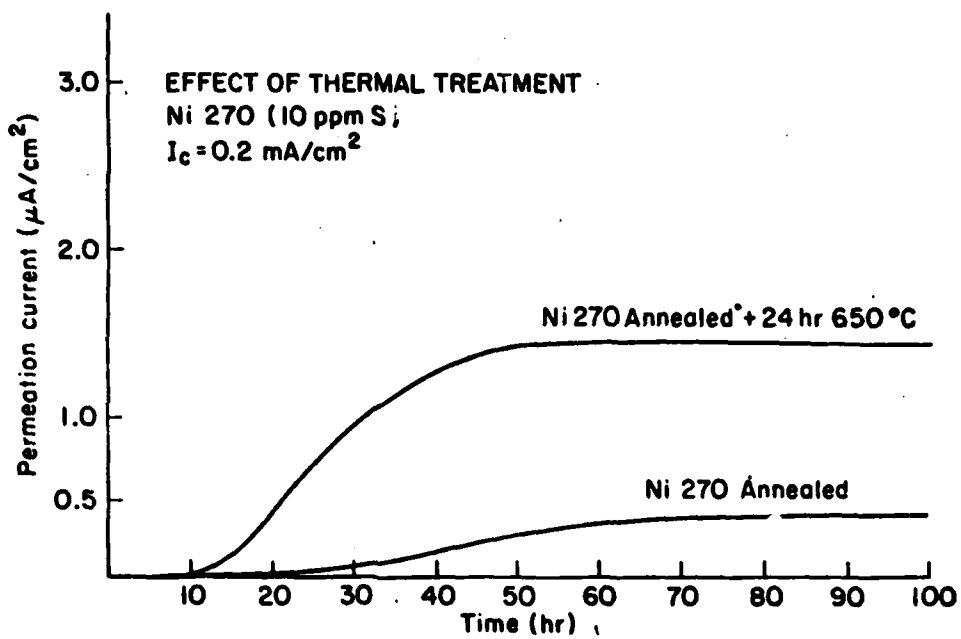


11a. $I_c = 0.2 \text{ mA}/\text{cm}^2$

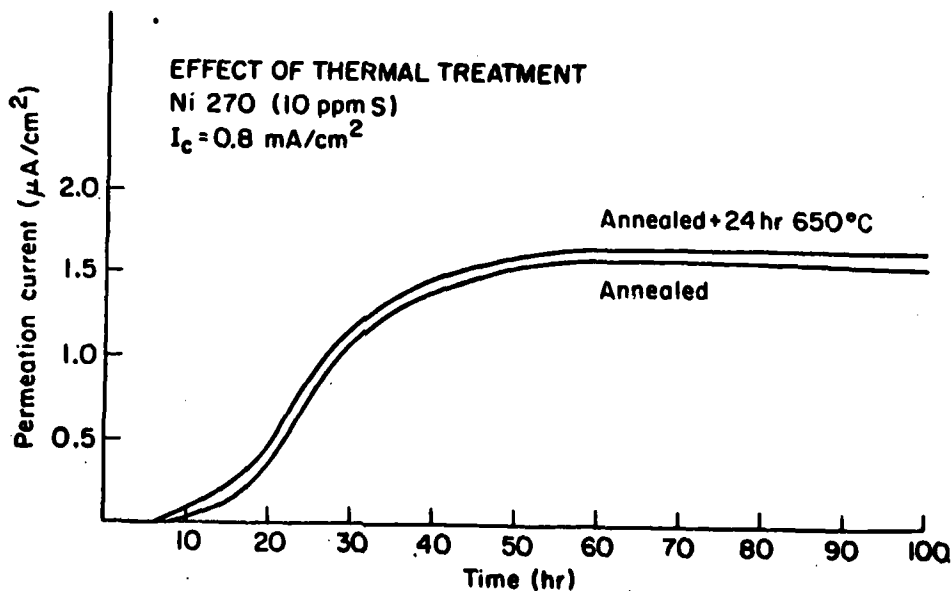


11b. $I_c = 0.8 \text{ mA}/\text{cm}^2$

FIGURE 11. Effect of thermal treatment on hydrogen permeability in Ni 200

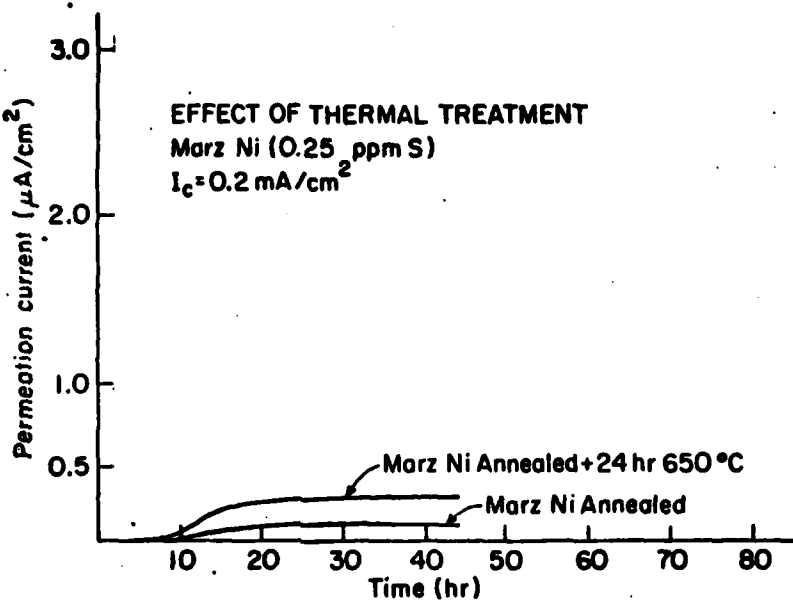


12a. $I_c = 0.2 \text{ mA/cm}^2$

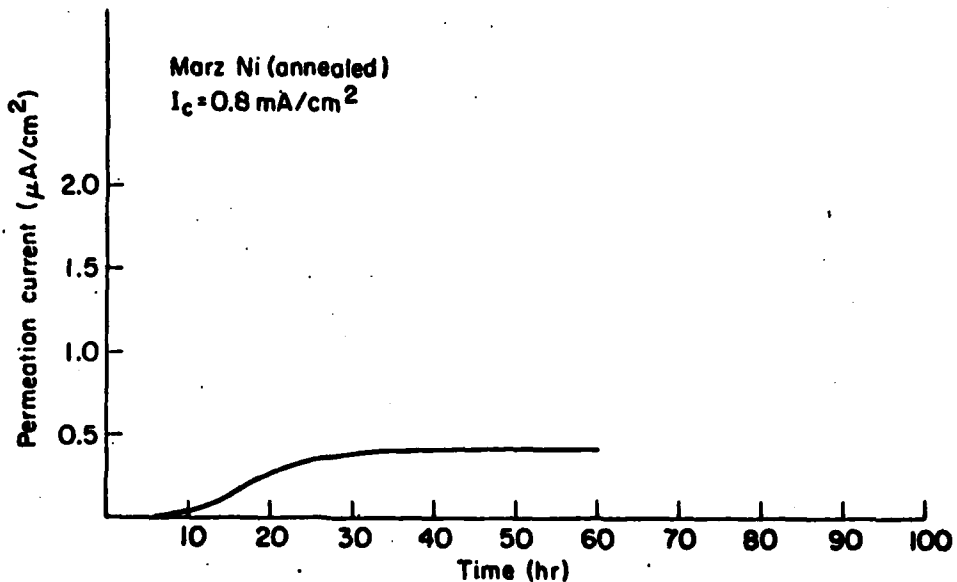


12b. $I_c = 0.8 \text{ mA/cm}^2$

FIGURE 12. Effect of thermal treatment on hydrogen permeability in Ni 270.



13a. $I_c = 0.2 \text{ mA/cm}^2$



13b. $I_c = 0.8 \text{ mA/cm}^2$

FIGURE 13. Effect of thermal treatment on hydrogen permeability in Marz Ni.

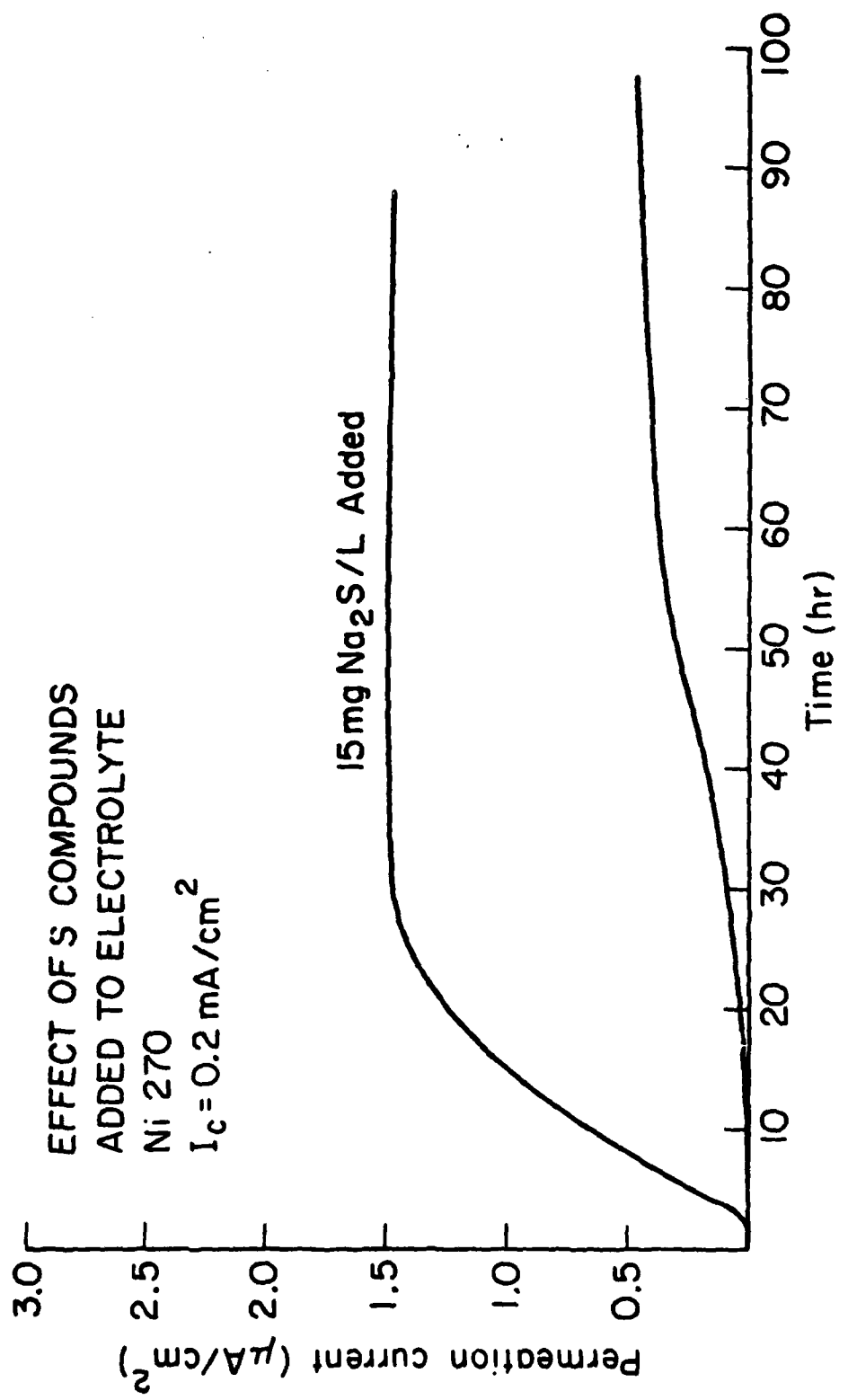


FIGURE 14. Effect of Na_2S on hydrogen permeability in Ni 270.

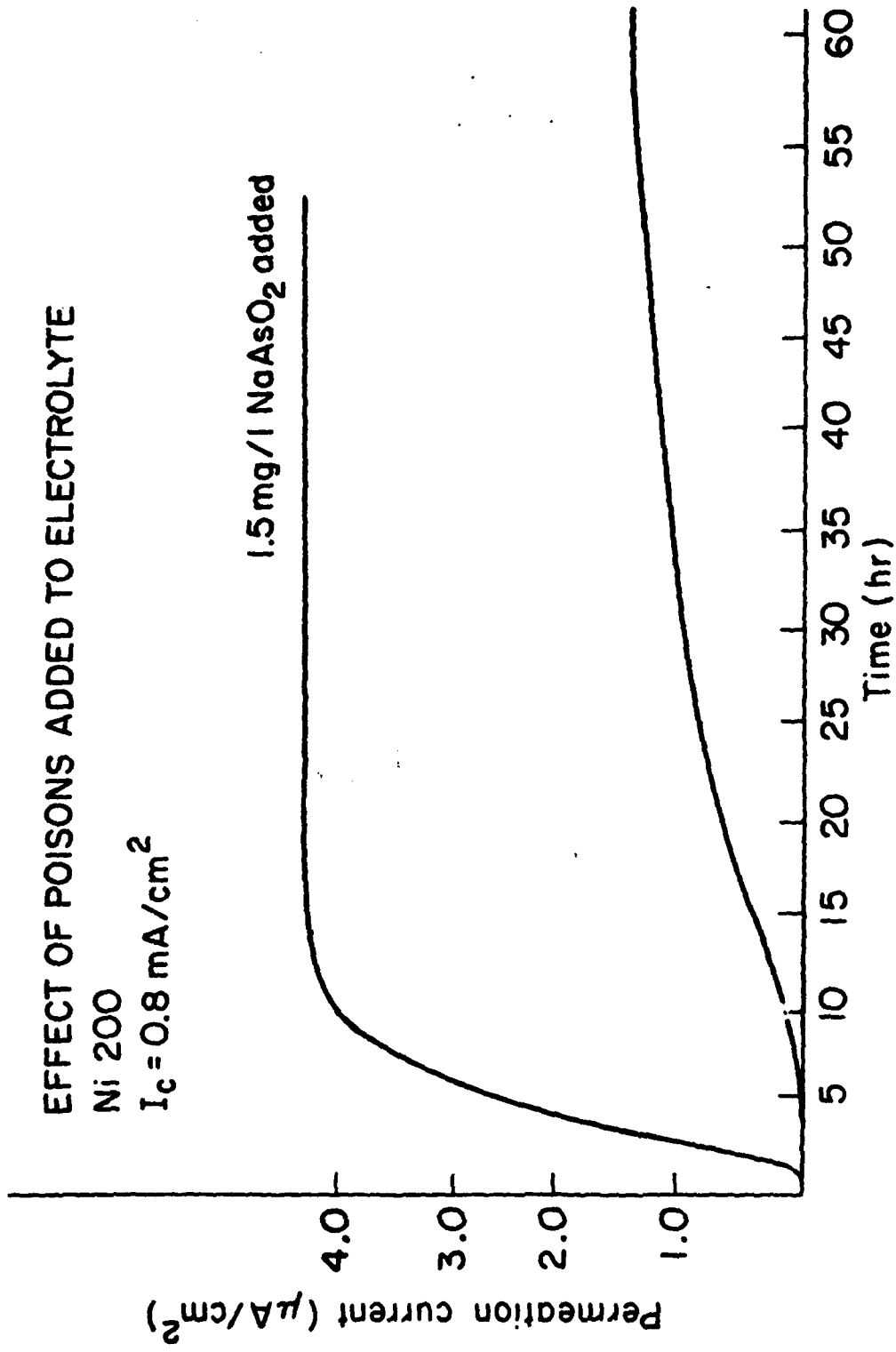


FIGURE 15. Effect of NaAsO₂ on hydrogen permeability in Ni 200.

TABLE IV
EFFECT OF GRAIN SIZE ON PERMEABILITY
AND DIFFUSION OF HYDROGEN

Grain Size	I_c (mA/cm^2)	D (cm^2/s)	J_∞ ($\mu\text{A}/\text{cm}^2$)
50 μm	0.8	3.3×10^{-10}	1.54
750 μm	0.8	3.3×10^{-10}	1.42

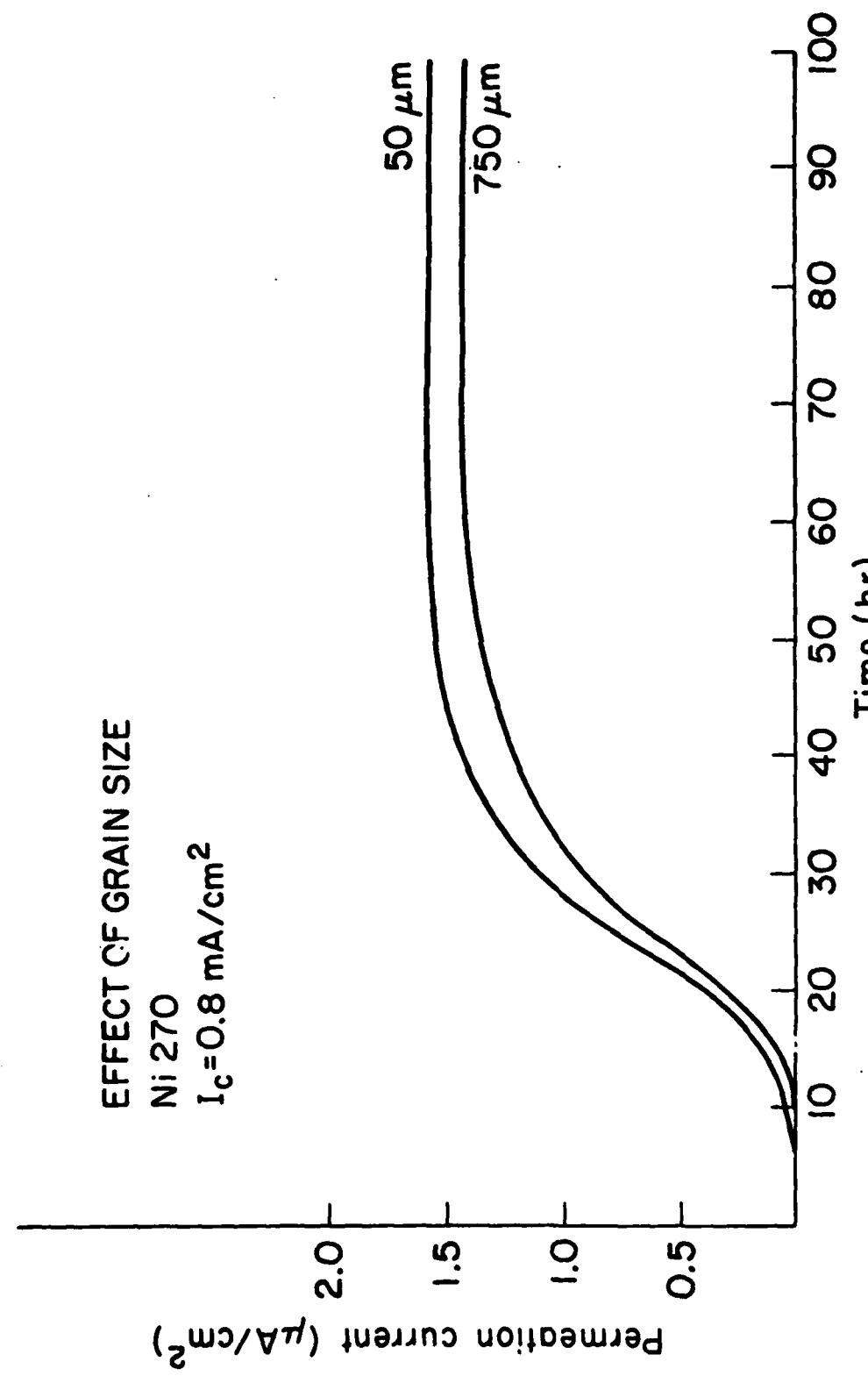


FIGURE 16. Effect of grain size on hydrogen permeability in Ni 270.

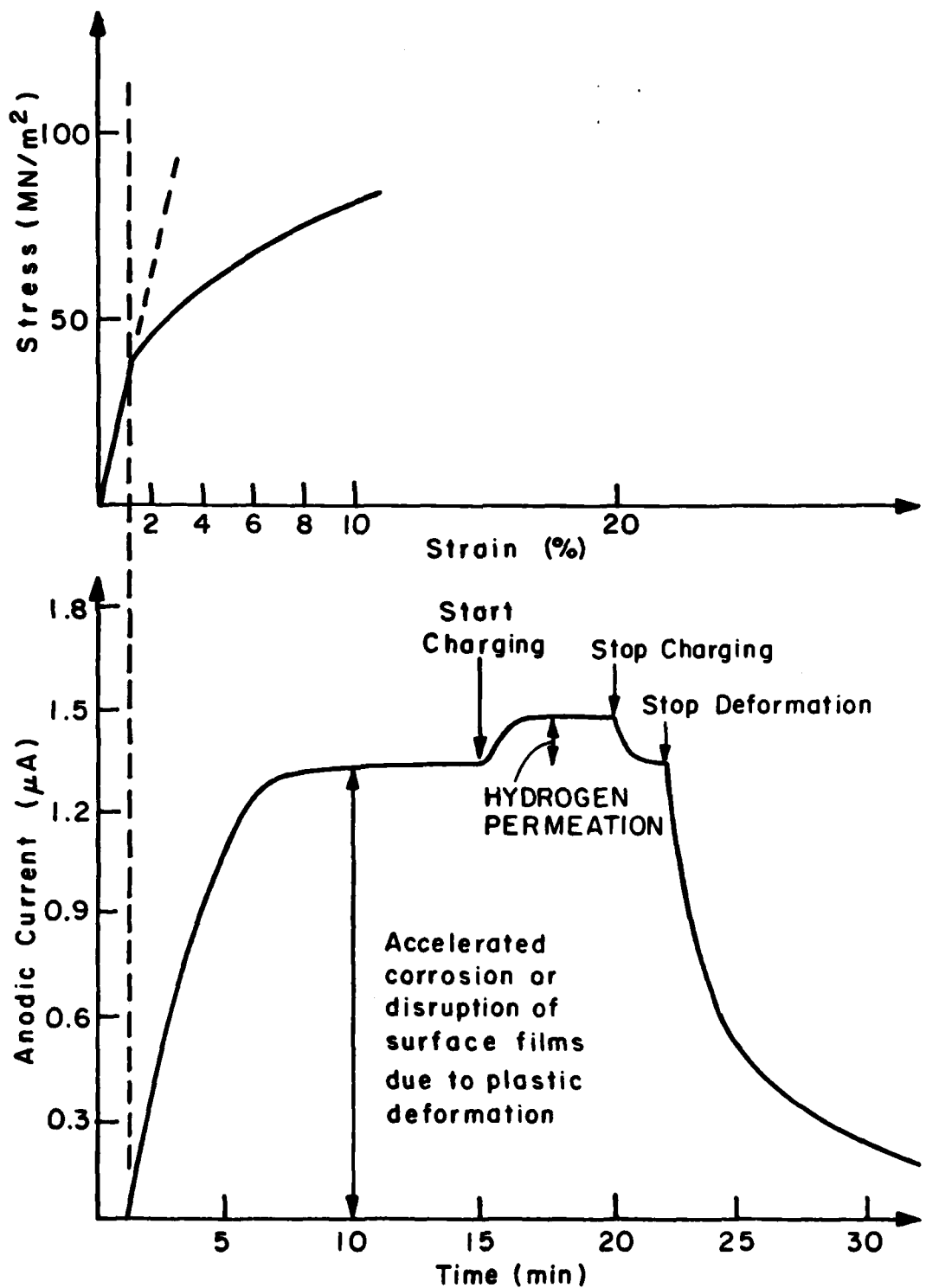


FIGURE 17. A schematic showing the steps involved in running a permeation experiment on a specimen undergoing plastic deformation.

experiment on a specimen undergoing plastic deformation. The material is solution annealed Ni 270 in all cases. After letting the anodic background current stabilize to a low value ($<0.1\mu\text{A}/\text{cm}^2$), deformation of the specimen is started using a constant extension rate (crosshead speed). At the onset of macroscopic plastic deformation, i.e., when the yield point is exceeded, there is an immediate increase in the anodic current. This increase is thought to be either due to disruption of surface films or accelerated anodic dissolution in the presence of plastic deformation. After some time, this current reaches a stable value (Figure 17) at which it can be maintained for 15-20 minutes. After attaining this steady background, the catholyte is poured into cathodic half-cell. At this point, any leaks are easily detected because they cause a change in the background current. Now hydrogen charging is started by polarizing the cathodic side galvanostatically. After 3 to 6 seconds, it is observed that the anodic current starts to rise and reaches a steady state value in less than a minute. When the charging current was switched off, the anodic current decayed to the value it had prior to charging. This observed transient is inversely proportional to the thickness of the specimen, which means that it is a volume effect, not a surface effect. This, coupled with theoretical predictions presented later and with the observed effects of various experimental parameters leads us to believe that the transient is due to hydrogen permeation and, more precisely, due to dislocation transport of hydrogen.

To further examine this, one might expect that different parameters which affect dislocation motion and the concentration of hydrogen should have an effect on the observed transient. Therefore, effects of strain rate, cathodic charging current, promoter additions to the electrolyte and metal grain size were studied. The results are presented in the following sections.

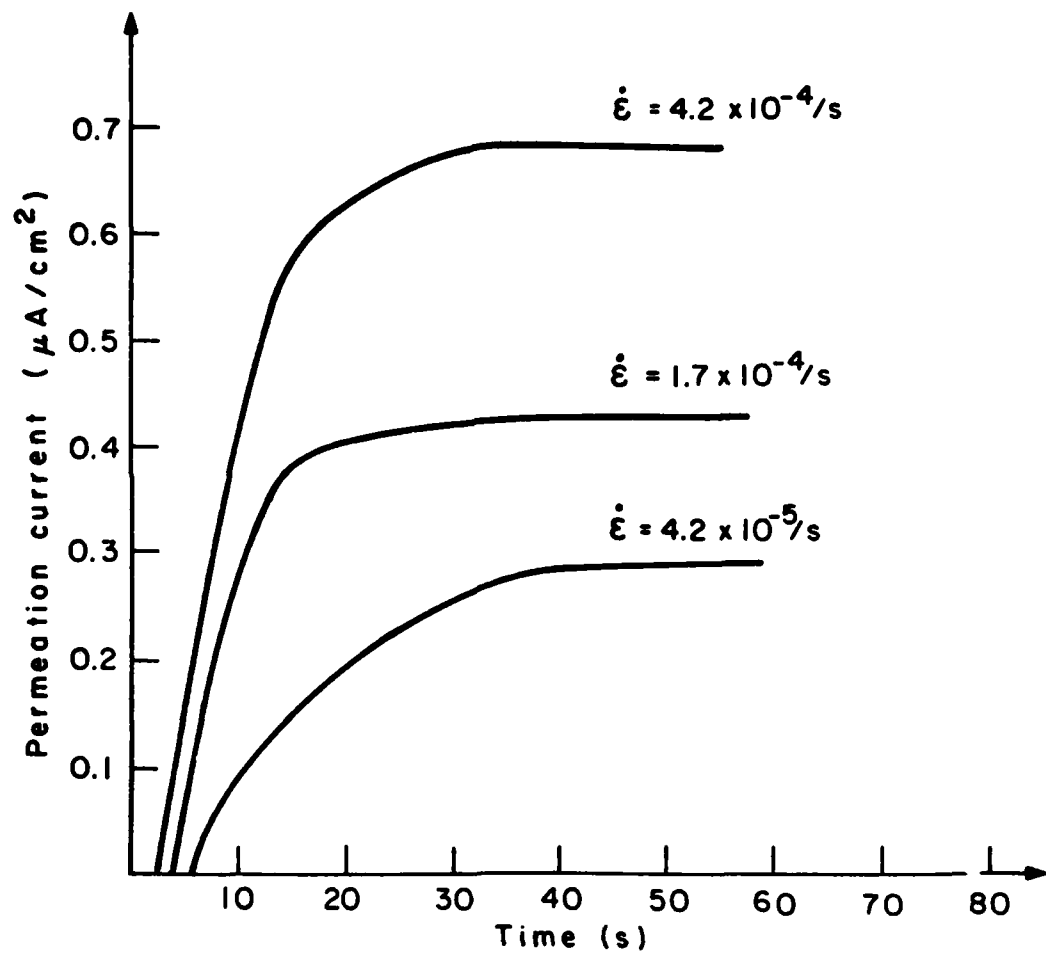
4.2.1 Effect of strain rate

The effect of strain rate on permeation by dislocation transport is shown in Figure 18. It can be seen that with increasing strain rate, the permeability also increases.

Also in this case, one can apply the permeation mathematics discussed earlier. If one determines the "effective diffusion coefficient" (diffusion coefficient of hydrogen in a metal undergoing plastic deformation), one obtains the results shown in Table V. The result is that the effective diffusivity is of the order of $10^{-5} \text{ cm}^2/\text{s}$. This is about five orders of magnitude higher than the hydrogen diffusivity in unstrained nickel. Tien et al., [3] have derived the following expression for the maximum penetration depth of hydrogen by means of dislocation transport

$$x_1 = (D/kT) (E_B/30b) t_p \quad (2)$$

where D is the diffusion coefficient, E_B the binding energy between the dislocation and its hydrogen atmosphere, 30b the



Effect of Strain Rate on Permeation Behavior. $I_C = 50\text{mA}$

FIGURE 18. Effect of strain rate on hydrogen permeability in Ni 270 undergoing plastic deformation.

TABLE V
HYDROGEN DIFFUSIVITY IN Ni 270
UNDERGOING PLASTIC DEFORMATION

$\dot{\epsilon}$ (1/s)	t_b (s)	$t_{1/2}$ (s)	D_{eff} (cm^2/s)
4.2×10^{-5}	5.5	14	1.8×10^{-5}
1.7×10^{-5}	4.0	10	2.6×10^{-5}
4.2×10^{-4}	2.5	8	3.2×10^{-5}

$\dot{\epsilon}$ = strain rate

t_b = break-through time

$t_{1/2}$ = half-rise time

D_{eff} = "effective" diffusion coefficient of H

effective interaction distance between the dislocation and this atmosphere and t_p the duration of plastic deformation. By means of lattice diffusion, the corresponding maximum penetration depth is

$$x_2 = 4\sqrt{Dt} \quad (3)$$

Taking the ratio x_1/x_2 and using literature values for E_B , 30b and D one obtains the following expression [3]

$$x_1/x_2 = 100\sqrt{t_p} \quad (4)$$

Applying equations (3) and (4) one can calculate that, according to the theory of Tien et al., it should take about 5 seconds for hydrogen to travel through the specimen thickness used in experiments of Figure 18. Examination of Table V shows breakthrough times varying between 2.5 and 5.5 seconds, in reasonable agreement with the theory.

One can also obtain decay transients in addition to the rise transients shown in Figure 18. This means that after the permeation transient has reached a steady state value, the charging current is switched off and the decay of the current back to its value prior to charging is recorded.

Figure 19 shows the decay transients for two different strain rates. In the case of the higher strain rate the decay is faster. In short, hydrogen travels out of the specimen faster.

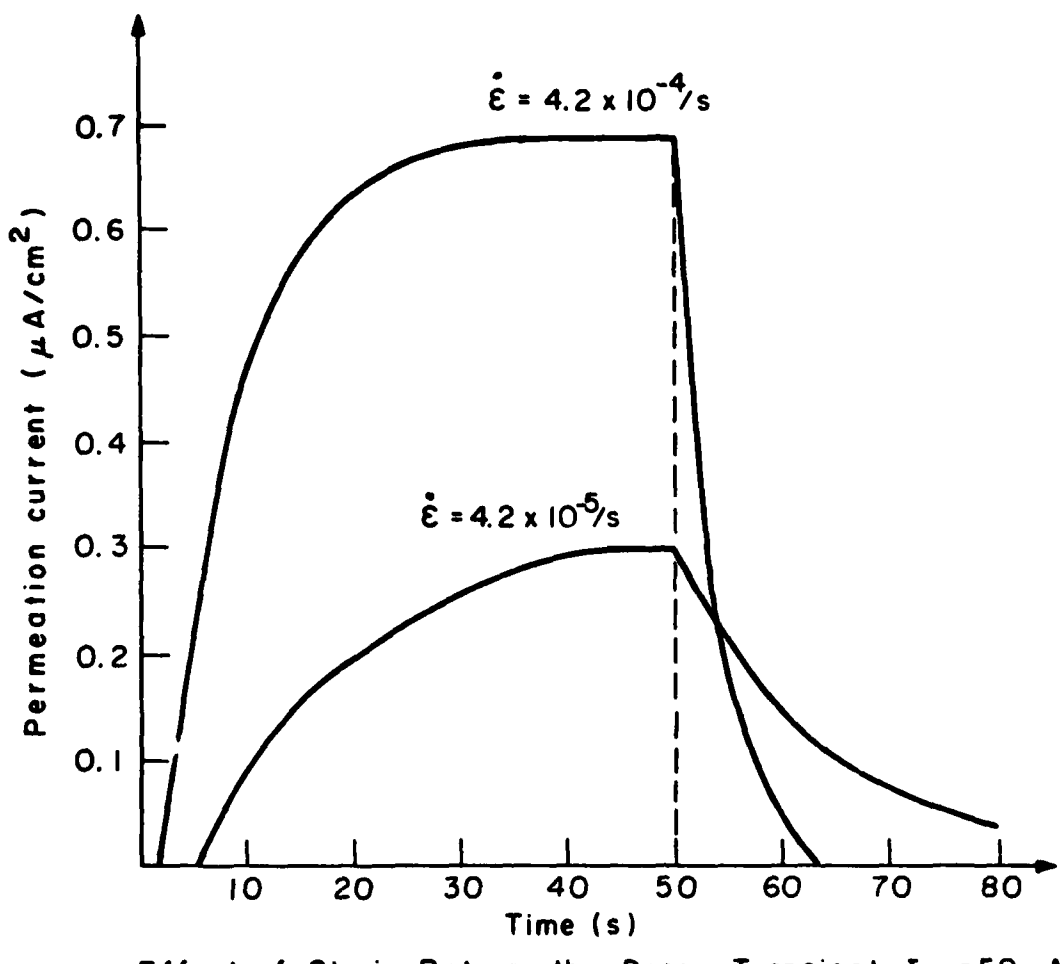


FIGURE 19. Effect of strain rate on decay transient (recorded on switching off the charging current).

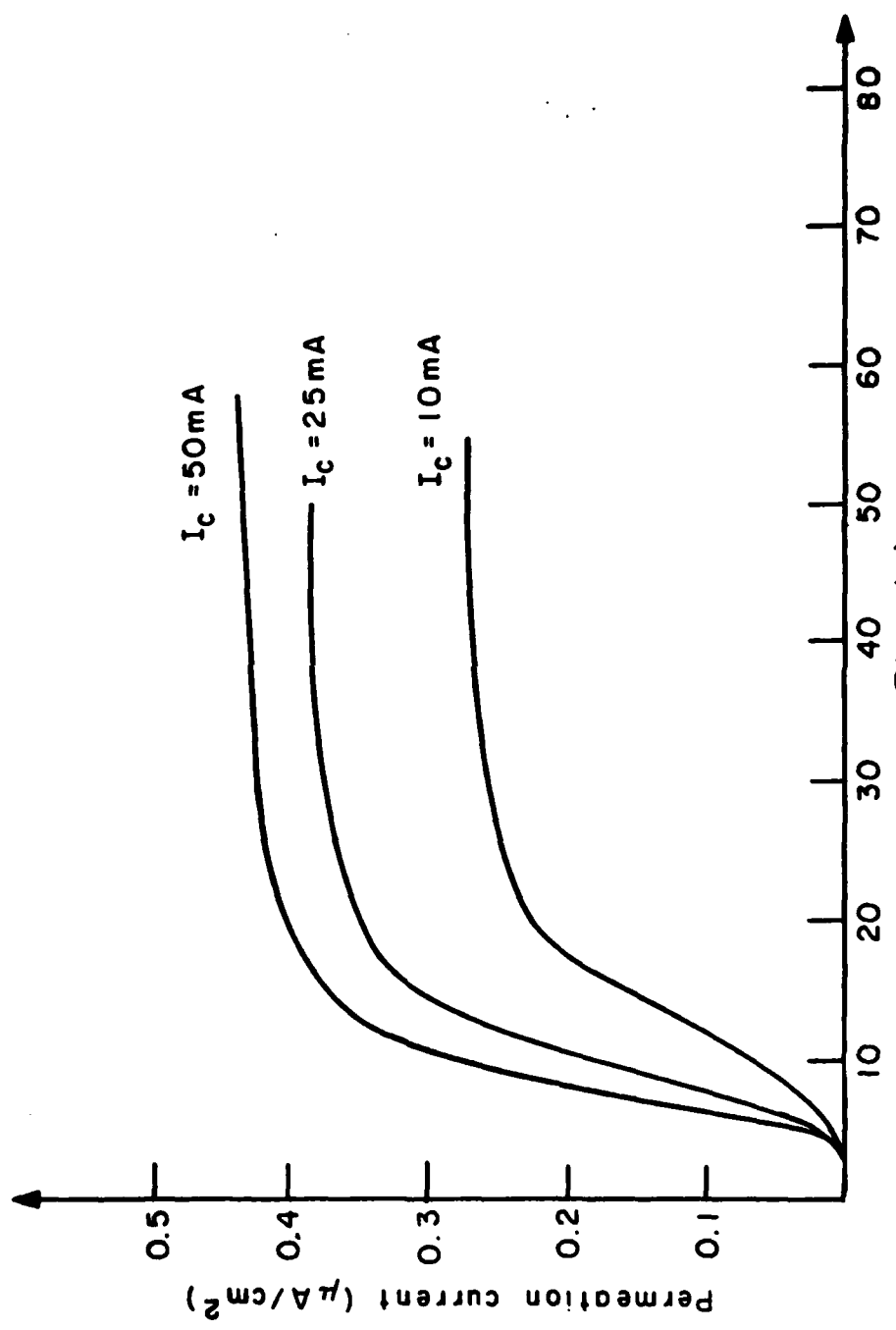
To obtain further support for the theory of Tien et al., one should be able to show that above a certain critical strain rate, $\dot{\epsilon}_c$, no dislocation transport takes place; i.e., the dislocations break away from their atmospheres. In the case of Ni, unfortunately, $\dot{\epsilon}_c$ is about $10^{-1}/s$ (3), far above the strain rates applicable in our permeation experiments (maximum about $10^{-4}/s$). Therefore, a metal or alloy where $\dot{\epsilon}_c$ is about $10^{-4} - 10^{-5}/s$ should be studied.

4.2.2 Effect of charging current

Effect of charging current on the permeation is shown in Figure 20. It can be seen that at higher charging current higher permeabilities are observed. This is due to the fact that the concentration of hydrogen in the specimen increases with charging current.

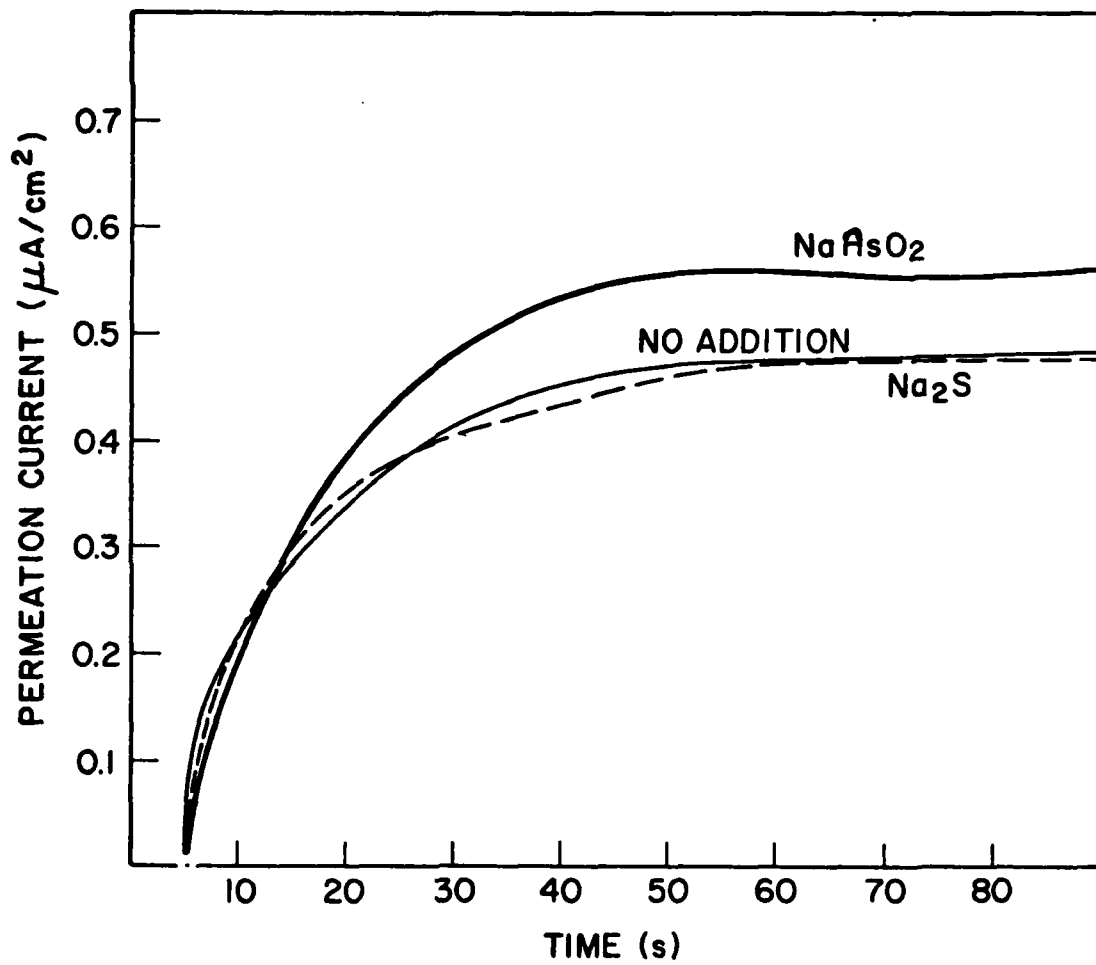
4.2.3 Effect of promoters

The absorption of hydrogen into unstrained nickel increases significantly in the presence of promoter elements in the electrolyte. Therefore, the effect of such elements on permeation when the metal is undergoing plastic deformation was studied. In one case 2.5mg/l NaAsO_2 and in the other 50 mg/l Na_2S were added. The results are shown in Figure 21. Na_2S had no effect at all. NaAsO_2 increases permeation slightly, but much less than



Effect of Charging Current on Permeation Behavior. Strain Rate = $1.7 \times 10^{-4}/\text{s}$

FIGURE 20. Effect of charging current on hydrogen permeability in Ni 270 undergoing plastic deformation.



EFFECT OF POISONS ADDED TO ELECTROLYTE
ON PERMEATION

$$\dot{\epsilon} = 8.3 \times 10^{-5}/\text{s}$$

$$I_c = 180 \text{ mA}/\text{cm}^2$$

FIGURE 21. Effect of promoter additions on hydrogen permeability on Ni 270 undergoing plastic deformation.

was the case in the absence of plastic deformation. This seems to indicate that plastic deformation somehow overrides the effect of promoters.

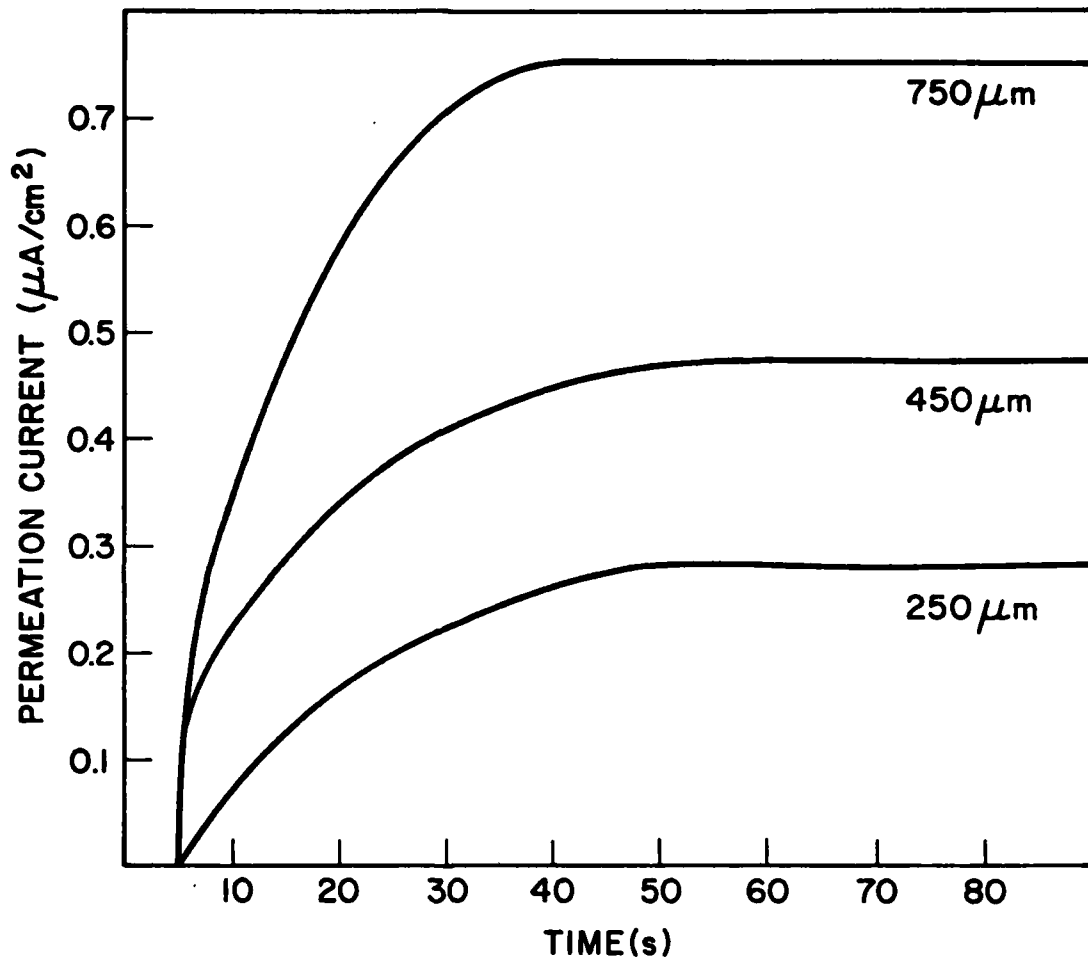
4.2.4 Effect of grain size

Dislocations cannot travel from one grain to another with their hydrogen atmospheres. When arriving at a grain boundary they are likely to "dump" the hydrogen there, and dislocations generated in the adjacent grain might then pick up the hydrogen. Based on this view, one might expect dislocation transport to be more efficient in a large grain size material where there are fewer obstacles for dislocation motion, i.e., the dislocations have a longer mean free path. Figure 22 shows results for three different grain sizes. The results agree with the predictions, i.e., the larger the grain size the higher the permeation flux.

4.3 Straining Electrode Experiments

4.3.1 Effect of applied potential

Table VI shows the plastic fracture elongation of Ni 270 annealed at 1100°C for 1 hour when the material was simultaneously strained and polarized at various potentials. It can be seen that at the open-circuit potential (-260mV SCE) and various anodic potentials (40, 300, 800mV SCE), the material had more or less the same fracture elongation as that when the material was fractured in air (50%). Potentials 40, 300 and 800mV SCE represent the active, active/pассив, and passive potentials of the material,



EFFECT OF GRAIN SIZE ON PERMEATION BEHAVIOR

$$\dot{\epsilon} = 8.3 \times 10^{-5}/\text{s}$$

$$I_c = 180 \text{ mA}/\text{cm}^2$$

FIGURE 22. Effect of grain size on hydrogen permeability in Ni 270 undergoing plastic deformation.

TABLE VI

EFFECT OF APPLIED POTENTIAL ON EMBRITTLEMENT
Ni 270; swaged 76%; annealed at 1100°C for 1 hr; deaerated 1N H₂SO₄

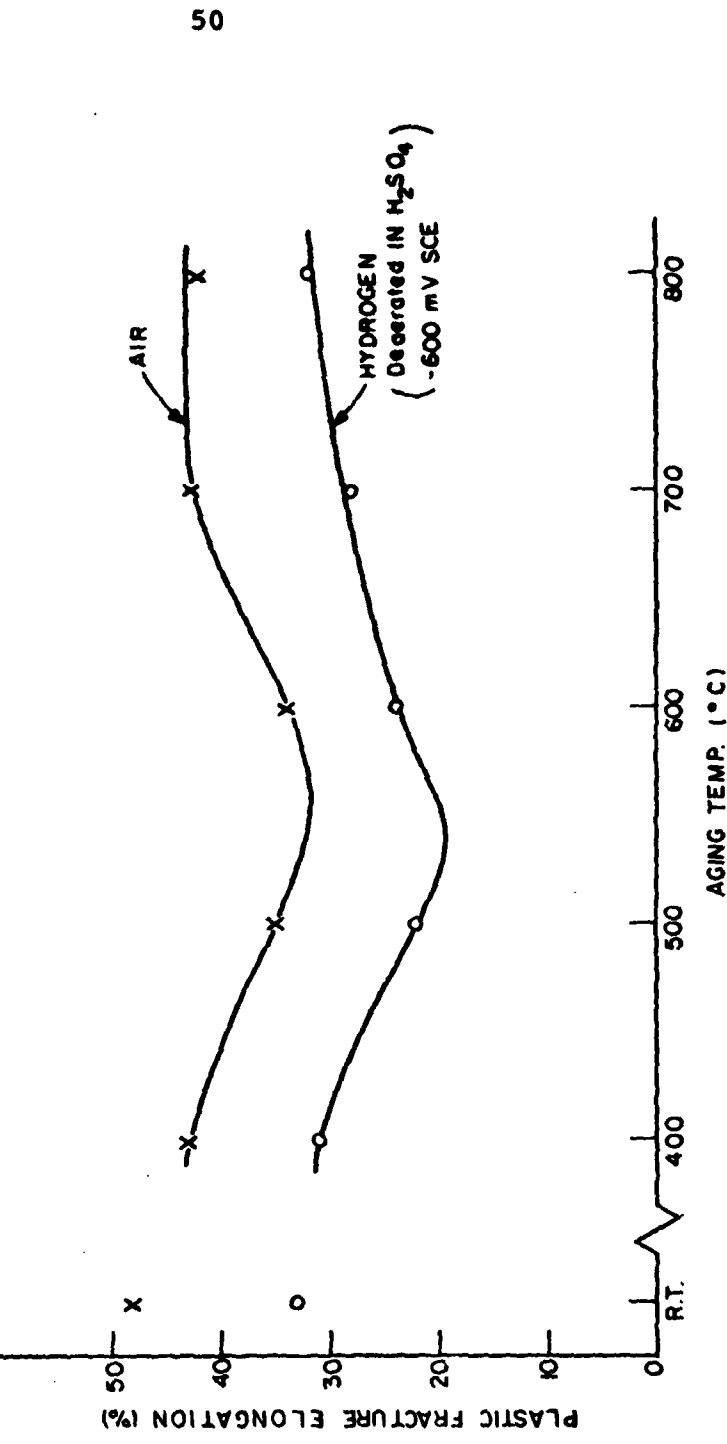
<u>E (mV SCE)</u>	<u>Fracture Elongation (%)</u>
-600	24
Open Circuit (-260)	47
+ 40	50
+300	53
+800	47
Air	50

respectively. However, the fracture elongation was drastically reduced to 24% when the material was polarized at the cathodic potential of -600mV SCE, i.e., in the presence of electrolytic hydrogen.

4.3.2 Effect of thermal treatment

Figure 23 shows the effect of low-temperature aging following the solution-annealing at 1200°C on the ductility of Nickel 200 (grain size 300 μ m) with and without hydrogen charging. The upper curve shows the fracture elongation of specimens broken in air (without hydrogen) and the bottom curve shows those when the specimens polarized at -600mV SCE (in the presence of hydrogen). When the aging temperature is designated as room temperature (R.T.) in the figure, the material was in the as-annealed condition. The fracture elongation values shown on the upper curve as compared to that of the as-annealed material broken in air indicate an embrittlement effect due solely to the aging treatment. The fracture elongations shown on the lower curve as compared to that of the as-annealed material broken in air indicate the embrittlement caused by aging and hydrogen-charging combined. It can be seen from the upper curve that subsequent aging treatments at various temperatures (400°C to 800°C) embrittled the annealed material even in the absence of hydrogen. However, in the presence of hydrogen-charging, the embrittlement effect was more profound (lower curve). Both upper and lower

FIGURE 23. EFFECT OF THERMAL TREATMENT ON EMBRITTLEMENT
Ni 200, swaged 70%;
annealed at 1200°C for 1 hr + 24 hr aging;
grain size 300 μ m



curves show a minimum (i.e., maximum embrittlement) when the material was aged at about 550°C.

Figure 24 shows the same data as in Figure 23 except that the Nickel 200 specimens were annealed at 1100°C instead, to produce a finer grain size of about 50 μm . Similar features of the aging effect can be observed here. Both aging and hydrogen-charging embrittled the material, and the embrittlement effects reached a maximum at the 550°C aging temperature. However, these fine-grained specimens were, in general, less susceptible to either aging or hydrogen-charging embrittlement than those of large grain size.

Similarly, Figure 25 shows the influence of aging temperature on the fracture elongation of Nickel 270 annealed at 1100°C (grain size 200 μm). For this purer material, annealed or annealed plus aged specimens broken in air had slightly higher ductilities (higher fracture elongations) than those of Nickel 200. But when the Nickel 270 specimens were broken in 1N H_2SO_4 at -600mV SCE, they were significantly more brittle (lower fracture elongations) than the Nickel 200 specimens. Both curves in Figure 25 show a minimum in fracture elongation at the 600°C aging temperature, but these minima are not as profound as those that appear in Nickel 200.

Tests were also done on Inconel 600 specimens, some of which were just annealed at 1200°C for 1 hour, and the others received additional aging at 700°C for 14 hours. The as-annealed and annealed plus aged specimens were broken in deaerated 1N H_2SO_4 at

FIGURE 24. EFFECT OF THERMAL TREATMENT ON EMBRITTLEMENT
 Ni 200; swaged 70%;
 annealed at 110°C for 1 hr. + 24 hr. aging;
 grain size 50 μ m

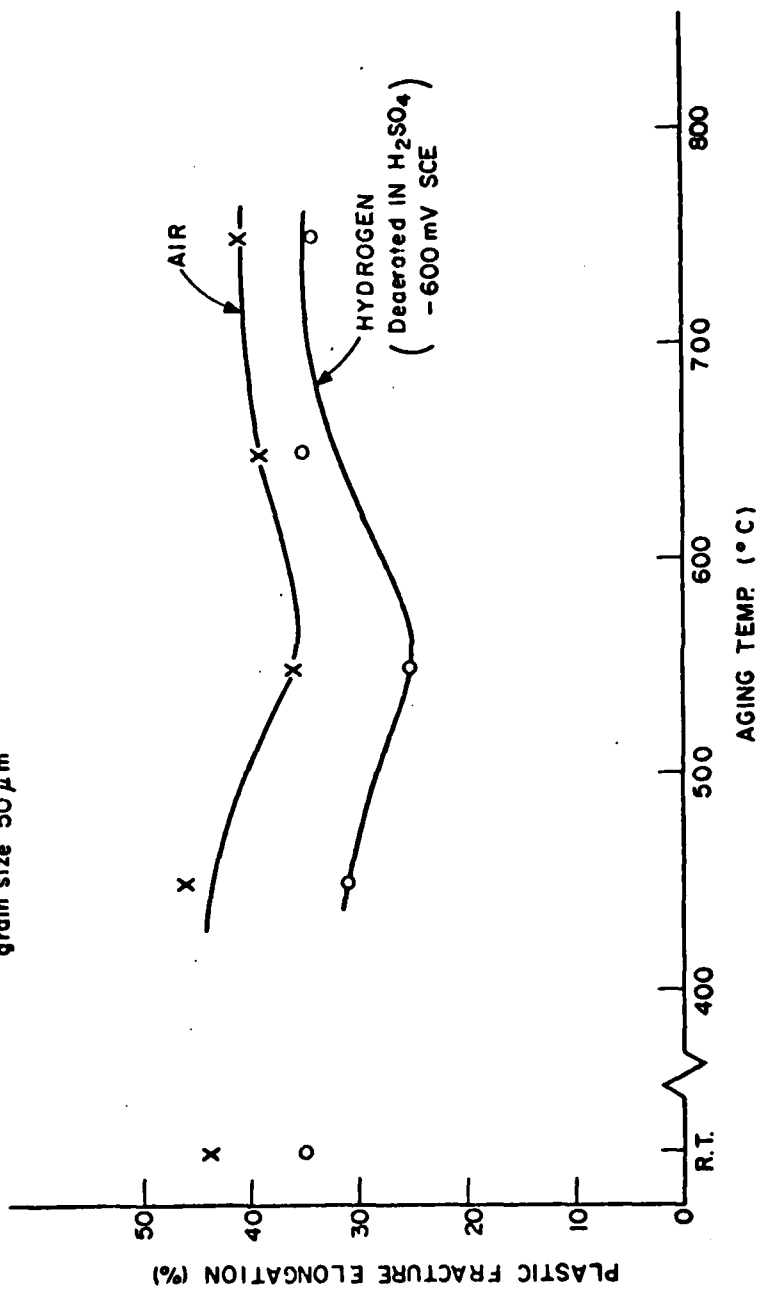
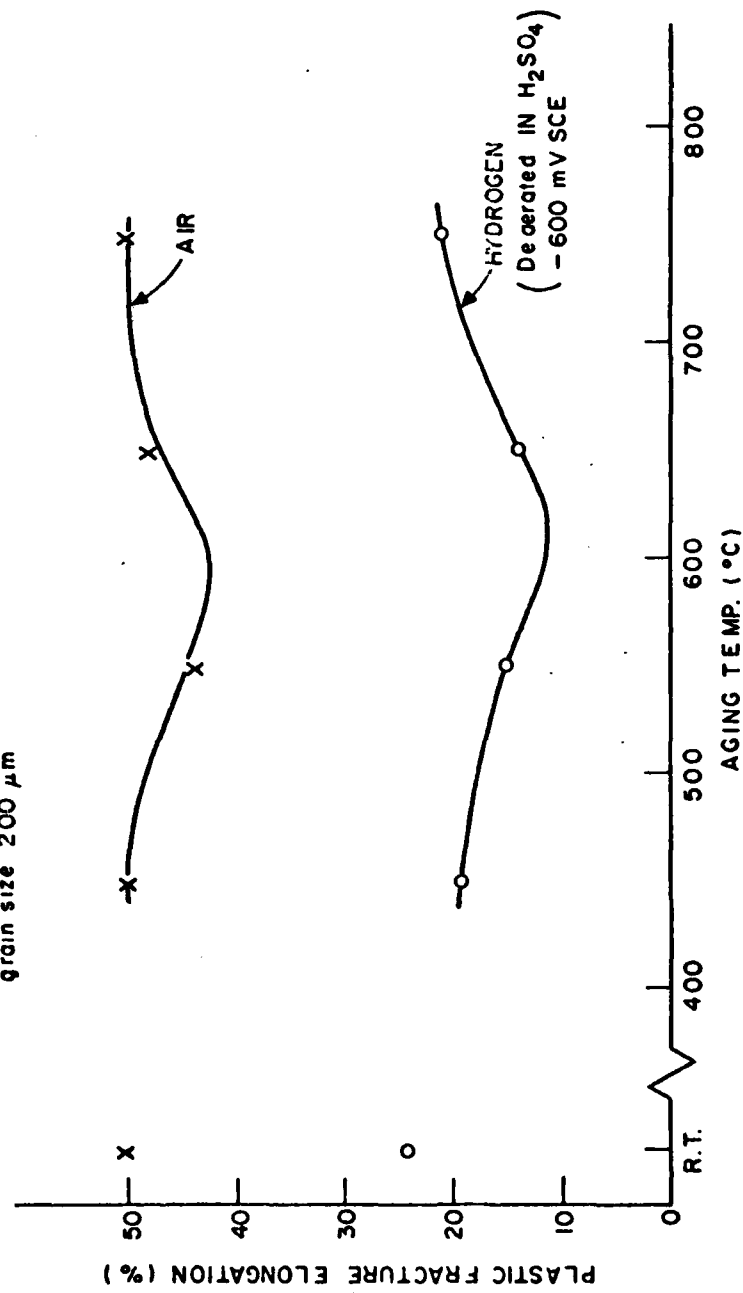


FIGURE 25. EFFECT OF THERMAL TREATMENT ON EMBRITTLEMENT

Ni 270; swaged 76%;
annealed at 1100°C for 1 hr. + 24 hr. aging
grain size 200 μm



-1000mV SCE as well as in air. The results are shown in Table VII. Embrittlement due to aging was obviously present in the nickel-base alloy. In the presence of hydrogen, both annealed and annealed plus aged specimens were significantly embrittled.

4.3.3 Effect of poison addition

NaAsO_2 is known as one of the hydrogen recombination poisons and at a concentration of 1 to 2mg/l in the electrolyte it was found in the permeation experiments that the hydrogen permeation through nickel was significantly increased. Hence, 1.5 mg/l NaAsO_2 was dissolved in the 1N H_2SO_4 electrolyte used in the straining electrode experiments performed on annealed Nickel 200 and Nickel 270, and their resulting ductilities are compared to those broken without the poison addition and those broken in air in Tables VIII and IX. From these data it is obvious that both Nickel 200 and Nickel 270 were more susceptible to hydrogen embrittlement when the poison was added to the electrolyte.

4.3.4 Effect of strain rate

In the majority of the straining electrode tests, the strain rate* was fixed at about $6 \times 10^{-5} \text{ s}^{-1}$. In order to investigate the effect of strain rate on the susceptibility to

*The strain rates reported here are actually the initial strain rates, or better termed, the elongation rates, since, in a strict sense, the strain rate is decreasing during the course of an ordinary tensile test with a constant cross-head speed.

TABLE VII
EFFECT OF THERMAL TREATMENT ON EMBRITTLEMENT
Inconel 600; swaged 85%

Heat Treatment	Fracture Elongation	
	In Air	In Deaerated 1N H ₂ SO ₄ (-1000mV SCE)
1200°C for 1 hr	47%	37%
1200°C for 1 hr +700°C for 14 hr	32%	21%

TABLE VIII
EFFECT OF POISON ADDITION ON EMBRITTLEMENT

Nickel 270; swaged 768; annealed at 1100°C for 1 hr

Environment	Fracture Elongation
Air	50%
Deaerated 1N H ₂ SO ₄ (-600mV SCE)	24%
Deaerated 1N H ₂ SO ₄ + 1.5mg/l NaAsO ₂ (-600mV SCE)	19%

TABLE IX
EFFECT OF POISON ADDITION ON EMBRITTLEMENT
Nickel 200; swaged 70%; annealed at 1200°C for 1 hr

Environment	Fracture Elongation
Air	48%
Deaerated 1N H ₂ SO ₄ (-600mV SCE)	33%
Deaerated 1N H ₂ SO ₄ + 1.5mg/l Na ₂ SO ₃ (-600mV SCE) ²	29%

hydrogen embrittlement, some experiments were run using strain rates 50 and 100 times as fast. Table X shows this fast strain rate effect for Nickel 200, annealed at 1200°C and aged at 550°C. Since the intrinsic ductility of a material changes with strain rate, an embrittlement index is used in order to compare the embrittlement susceptibilities at various strain rates. The embrittlement index shown in Table X is defined as

$$\text{E.I.} = \frac{(\text{Fracture elongation in air}) - (\text{Fracture elongation in hydrogen})}{(\text{Fracture elongation in air})}$$

From the table one can see that when the annealed plus aged Nickel 200 was fractured in hydrogen at a strain rate $6 \times 10^{-5} \text{s}^{-1}$, the E.I. was equal to 0.38, whereas the E.I. was reduced to about 0.20 when the strain rate was increased to 50 and 100 times as fast. In other words, hydrogen embrittlement was less severe at the higher strain rates.

4.3.5 Fracture mode

From the observation on the fracture surfaces in the scanning electron microscope, it was found that Nickel 270 broken in the straining electrode experiments cracked almost 100% intergranularly when polarized at a cathodic potential (i.e., in the presence of a hydrogen source). In other conditions, in air or at other anodic potentials with the material aged or not, Nickel 270 fractured in a transgranular dimpled rupture

TABLE X
EFFECT OF STRAIN RATE ON EMBRITTLEMENT

Nickel 200; swaged 70%; annealed at 1200°C for 1 hr;
aged at 500°C for 24 hr; broken in air or in deaerated 1N H₂SO₄ (-600mV SCE)

Initial Strain Rate	Embrittlement Index
$6 \times 10^{-5} s^{-1}$	0.38
$3 \times 10^{-3} s^{-1}$	0.21
$6 \times 10^{-3} s^{-1}$	0.19

manner. For Nickel 200 and Inconel 600, the fracture mode was a mixture of intergranular and transgranular fractures when polarized cathodically during straining. There was a positive correlation between the extent of intergranular fracture and the degree of hydrogen embrittlement (as measured by the reduction in fracture elongation). The materials fractured transgranularly in air under all heat treatment conditions. Figure 26 shows the SEM micrographs of different kinds of fracture surfaces obtained.

Some experiments were performed on Nickel 270 and Nickel 200 which were pre-charged with hydrogen prior to the tensile testing. Tensile specimens were pre-charged in 1N H_2SO_4 + 1.5mg/l $NaAsO_2$ solution at about $10mA/cm^2$ for 165 hours, and were then fractured in air. In contrast to those specimens simultaneously strained and charged in the straining electrode tests (without pre-charging) which showed more or less uniform features throughout the whole fracture surface, the pre-charged specimen had a fracture surface which was intergranular (in the case of Nickel 270) or intergranular/transgranular (in the case of Nickel 200) in the outer-ring region, and was transgranular mixture in the central area. Moreover, the pre-charged specimens had numerous secondary cracks along the gauge section besides the main crack that had led to fracture. On the other hand, the secondary cracks were largely absent in specimens broken in the straining electrode experiments.



FIGURE 26a. Fracture surface of Ni 270 broken in air, 60x.



FIGURE 26b. Fracture surface of Ni 270 broken in deaerated
1N H_2SO_4 at -600mV SCE, 60x

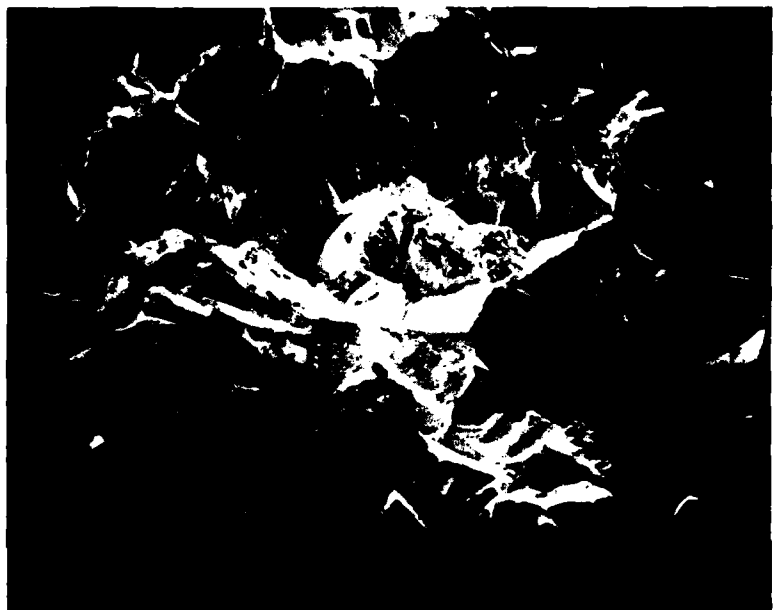


FIGURE 26c. Fracture surface of Ni 200 broken in deaerated
1N H_2SO_4 at -600mV SCE, 60x.



FIGURE 26d. Fracture surface of Ni 270 precharged at 10mA/cm^2 for 165 hr and broken in air, 60x.

4.4 Cathodic Polarization Curves

4.4.1 Effect of thermal treatment

To study the effect of thermal treatment in the range of impurity segregation on cathodic polarization kinetics, galvanostatic cathodic polarization curves were determined for Ni 270 and Ni 200 in both the annealed and annealed + thermally treated conditions. The curves for Ni 270 are presented in Figure 27 and the curves for Ni 200 in Figure 28. The following observations can be made:

- all curves obey linear Tafel kinetics with the slope varying between -120 and -130mV/decade
- deviation from linear kinetics due to concentration polarization is observed at current densities higher than 10 mA/cm^2
- for both Ni 270 and Ni 200, the curves shift slightly towards more negative values as a result of the thermal treatment. However, these shifts are within experimental error so that the thermal treatment does not seem to have any significant effect
- by extrapolating the linear part of the curve to the reversible hydrogen potential one obtains a value of about $9 \times 10^{-6} \text{ A/cm}^2$ for the exchange current density for H_2 evolution ($\log i_{\text{O},\text{H}} = -5.0$) which is fairly close to a reported literature value of $\log i_{\text{O},\text{H}} = -5.3$ [36].

As a summary, thermal treatment to produce grain boundary segregation does not affect overall "macroscopic" polarization

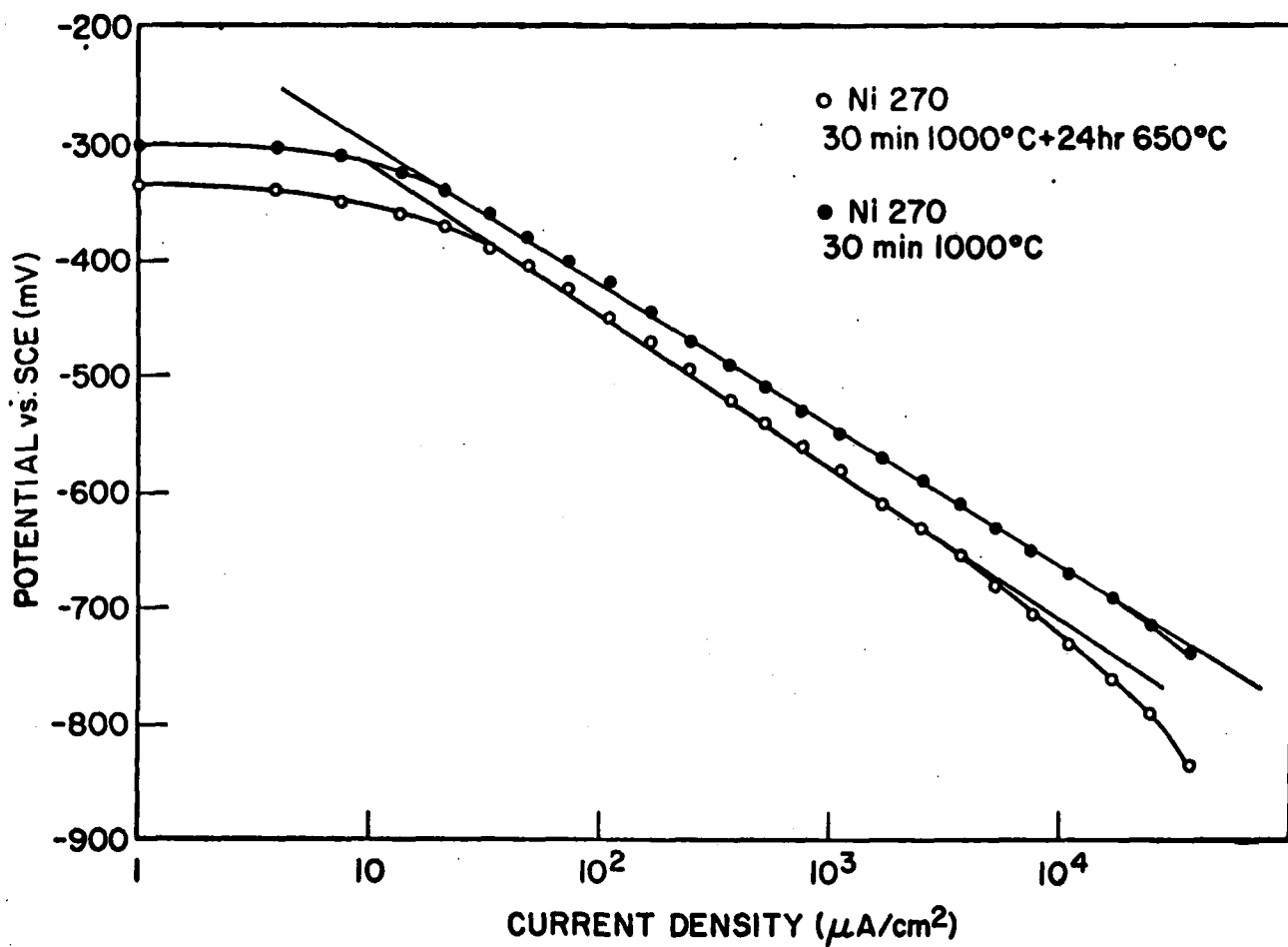


FIGURE 27. Effect of thermal treatment on cathodic polarization behavior of Ni 270 in 0.1N H_2SO_4 .

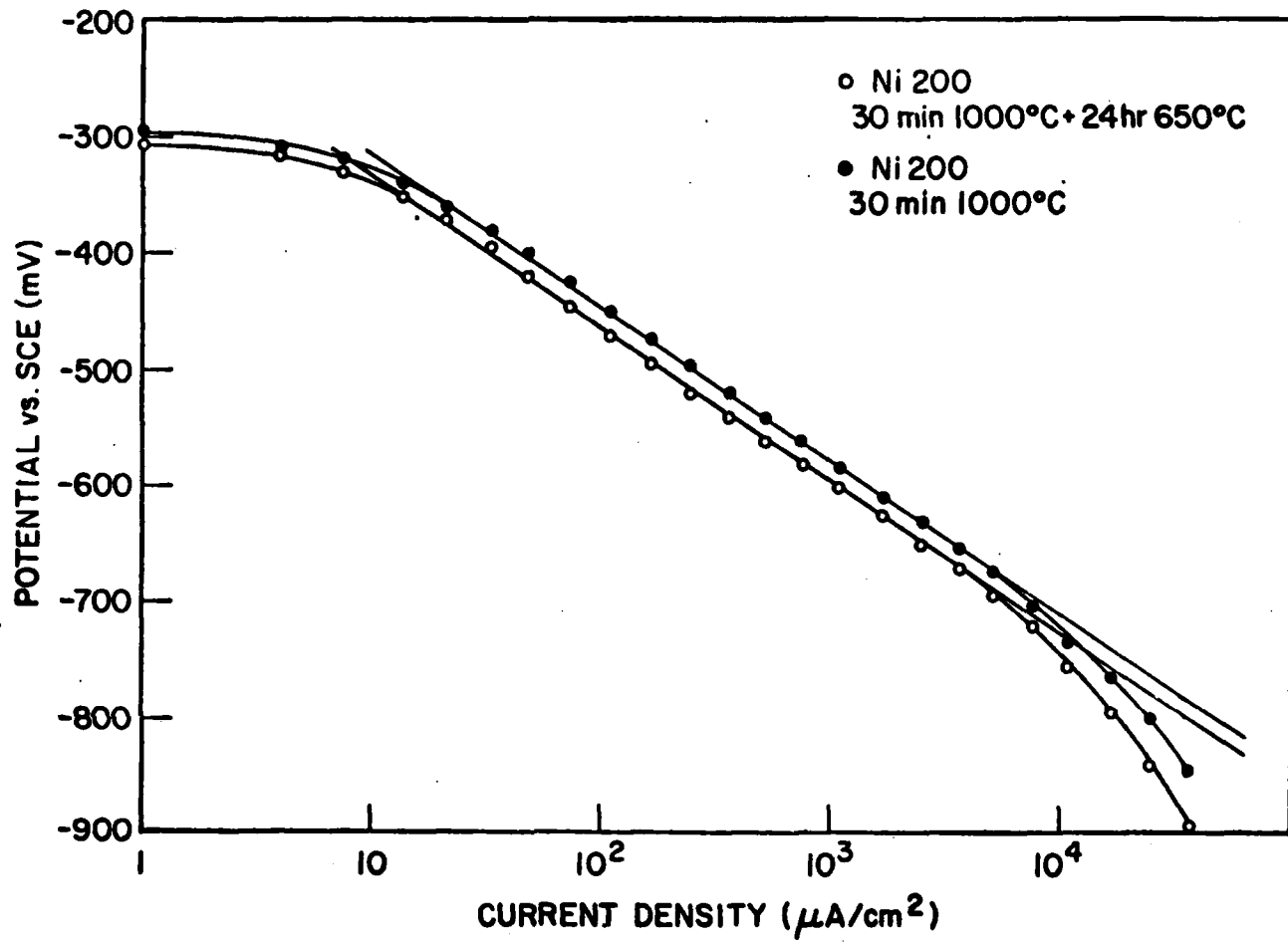


FIGURE 28. Effect of thermal treatment on cathodic polarization behavior of Ni 200 in 0.1N H_2SO_4 .

behavior. This is to be expected since the fraction of the total surface area which is grain boundary is very low.

4.4.2 Effect of promoter additions

Following additions of different promoters from the group V-A and VI-A groups were made to the 0.1N H_2SO_4 solution: 30mg/l Na_2S , 10 mg/l Na_2SeO_3 , 10 mg/l $NaAsO_2$ and 1.5 mg/l Sb_2O_3 . The cathodic polarization curves are shown in Figure 29. Two trends can be detected:

- group V-A elements As and Sb increase the hydrogen overpotential corresponding to a certain current density and decrease the overall kinetics (current density corresponding to a certain potential decreases)
- group VI-A elements S and Se accelerate the overall kinetics and decrease the hydrogen overpotential

Na_2S and Na_2SeO_3 additions shifted the open circuit potential in the more active direction, $NaAsO_2$ in the more noble direction. The addition of Sb_2O_3 was so small that it did not affect the open circuit potential.

As a summary, it seems that even if both group V-A and VI-A elements enhance the absorption of hydrogen, the mechanisms of this enhancement are different, at least judging from the polarization curves.

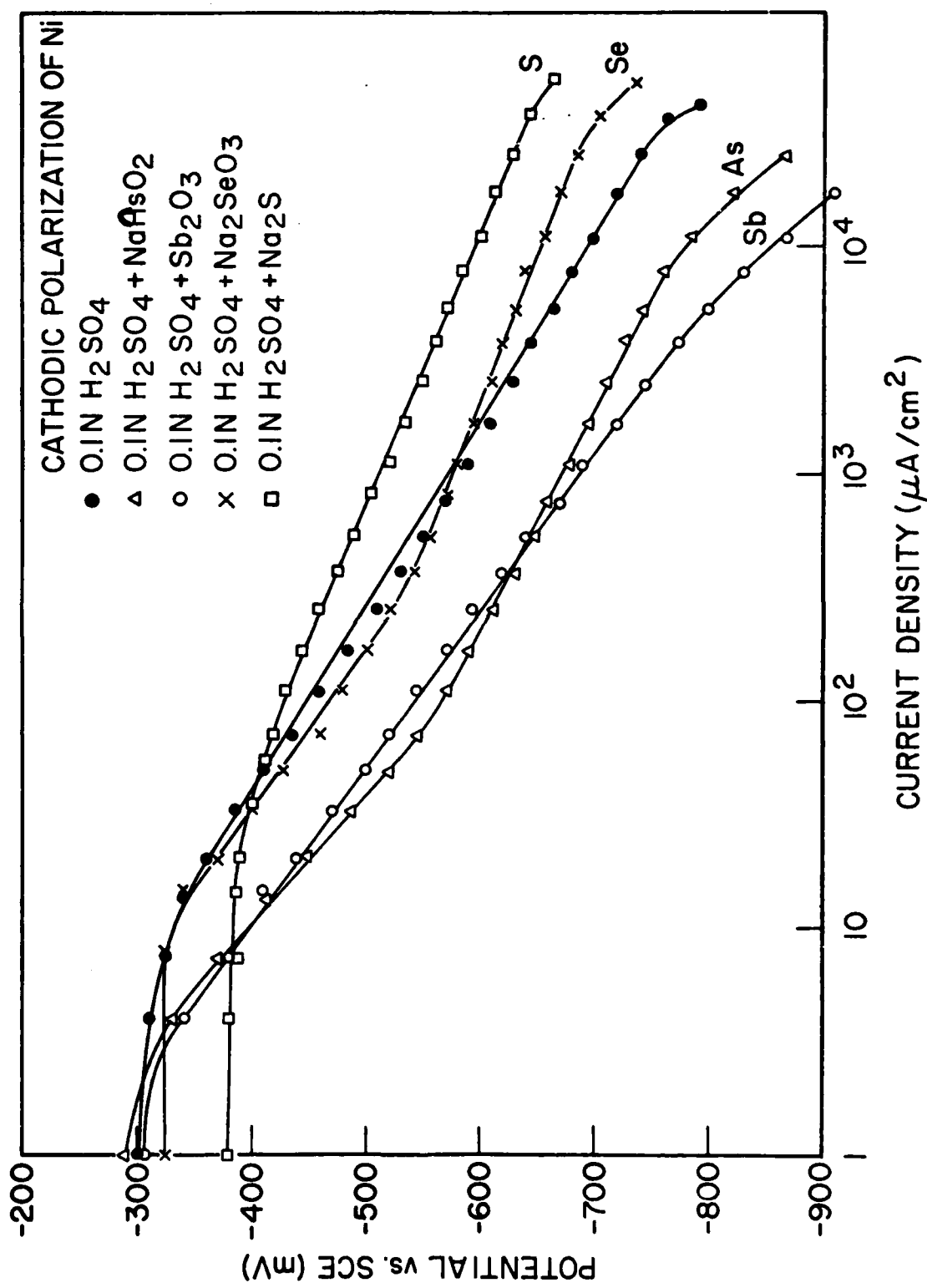


FIGURE 29. Effect of different poison on cathodic polarization behavior in 0.1N H_2SO_4 .

4.5 Grain Boundary Electrode Potential Measurements

Grain boundary segregation may create a galvanic difference between the segregated grain boundary and the grain interior which might have implications on the cracking phenomenon. It was, therefore, considered useful to compare the corrosion potentials of "pure" and segregated grain boundaries with that of the matrix. Therefore, specimens were heat treated as shown in Table XI, they were subsequently charged with hydrogen and fractured intergranularly in an Instron machine. After fracture, open circuit potentials of the fracture surfaces were immediately determined. The results are shown in Table XI. Solution annealing at 1000°C and subsequent thermal treatment at 700 and 800°C does not result in any change as compared with the corrosion potential of the matrix. It is reasonable to assume that the open circuit potential of a ductile fracture surface is representative of the potential of the matrix and the open circuit potential of an intergranular fracture surface representative of that grain boundary. However, thermal treatment at 400, 500 and 600°C results in a 70mV shift in the active direction. Significantly, these are also temperatures at which segregation takes place [27]. As a check, some specimens were exposed to the laboratory atmosphere for 1 hr before the open circuit potential determination. The resultant corrosion potential in this case was -180mV SCE presumably due to an oxide film formed on the fracture surface. This suggests that an analysis of the fracture surface within 1 hr of fracture does not result in substantial film

TABLE XI
OPEN CIRCUIT POTENTIALS OF GRAIN BOUNDARIES
IN Ni 270 AS A FUNCTION OF HEAT TREATMENT

Heat Treatment	Electrode Potential (mV SCE)
30 min 1000°C	-425 mV
30 min 1000°C + 24h 400°C	-490 mV
30 min 1000°C + 24h 500°C	-490 mV
30 min 1000°C + 24h 600°C	-495 mV
30 min 1000°C + 24h 700°C	-420 mV
30 min 1000°C + 24h 800°C	-410 mV

Comparison: ductile fracture surface

$$E_{corr} = -410 \text{ mV}$$

growth (open circuit potential -410- -490mV SCE) and that we have an essentially "fresh" fracture surface.

It is interesting to note that the open circuit potentials of the fresh fracture surfaces were about 100mV more active than the corresponding values of bulk specimens. Possibly, this is due to plastic deformation which might make the fracture surfaces more active, e.g., due to a higher dislocation density.

As a summary, the open circuit potential measurements showed that thermal treatment in the range for grain boundary segregation creates a galvanic difference between the grain boundary and the matrix. This difference might give rise to local action currents which might stimulate the entry of hydrogen into the metal.

5. DISCUSSION

5.1 Dislocation Transport of Hydrogen

The permeation experiments performed on Ni 270 undergoing plastic deformation showed that hydrogen can travel in nickel undergoing plastic deformation at rates five decades higher than the lattice diffusion rate. Experimentally observed rates were in good agreement with the theory of Tien et al [3]. In addition, effects of strain rate, charging current, promoter additions and grain size gave further support to the theory.

In considering the effects of strain rate and grain size on dislocation transport of hydrogen, a good starting point is the basic equation

$$\dot{\epsilon} = \rho b v \quad (5)$$

where $\dot{\epsilon}$ is the strain rate, ρ the dislocation density, b the Burgers vector and v the dislocation velocity. Equation (5) can also be written in the following form

$$\dot{\epsilon} = \rho b \lambda / t \quad (6)$$

where λ is the dislocation mean free path and t the time between "collisions." When the dislocations encounter obstacles such as grain boundaries, particles or inclusions they may dump their hydrogen at these points. The hydrogen can then be picked up by other dislocations or it can be trapped at grain boundaries,

particle-matrix interfaces, etc. Thus, factors affecting dislocation motion should also affect dislocation transport.

The effect of strain rate can be considered in terms of equation (5). If $\dot{\epsilon}$ increases, ρ and/or v has to increase as well. If the number of such "active" dislocations increases, the permeation flux also should increase as was observed (Figure 18). Also, if the average dislocation velocity increases, the permeation flux should increase. The decay transient results can also be interpreted in terms of dislocation velocity (Figure 19). The faster decay in the case of a high strain rate is due to the faster exit of hydrogen out of specimen because the average dislocation velocity is higher. Another possible way to explain the results of Figure 18 is that with increasing strain rate, the amount of absorbed hydrogen increases.

The effect of grain size can also be considered in the light of equation (6). The mean free path, λ , depends on the grain size of the metal. In a large grain size metal, λ is longer than in a small grain size metal; that means that the dislocations are able to travel longer distances without encountering obstacles (mainly grain boundaries). So, in a large grain size material one might expect a higher dislocation transport efficiency. This, in fact, was observed (Figure 22). Tien et al., [3] have done calculations based on their model and consider the parameter $\rho\lambda$ as a kind of measure of hydrogen transport efficiency. Figure 30 shows the results of their calculations which predict a higher efficiency for large grain

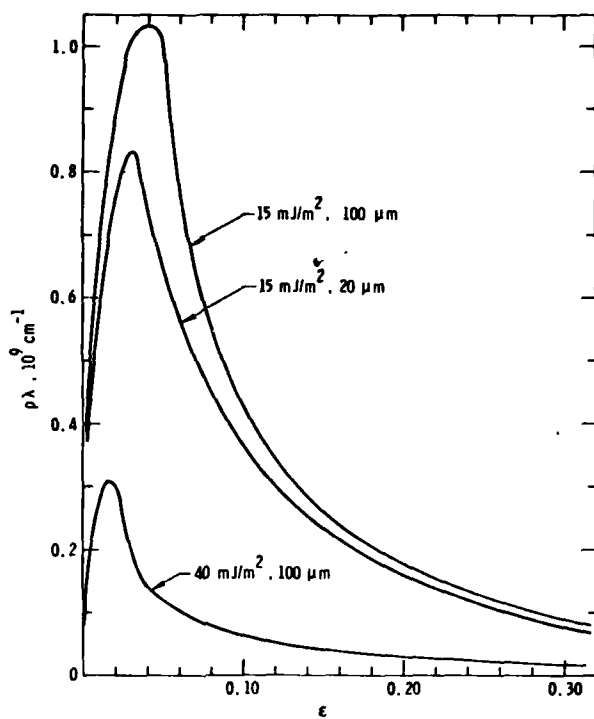


FIGURE 30. Effect of grain size and stacking fault energy on the hydrogen transport efficiency by the dislocation mode according to the model by Tien et al. [3].

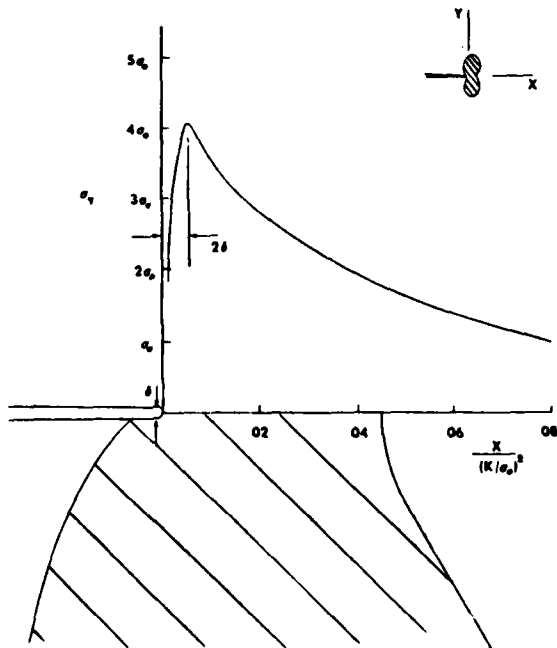


FIGURE 31. Stress distribution and plastic zone ahead of a propagating crack according to Rice [38].

sizes. Even more significant should be the role of stacking fault energy. The lower it is the higher the efficiency of hydrogen transport. It would be interesting to investigate this idea by using stainless steels in which one can get a wide range of stacking fault energies with very small composition changes. Work by Louthan et al., [22] has shown that hydrogen-dislocation interactions occur in stainless steels, so a dislocation transport mode might operate.

It is generally observed that a large grain size is more deleterious for hydrogen resistance [1]. One could speculate that this might be due to a higher efficiency of dislocation transport of hydrogen. The same kind of reasoning could apply for stacking fault energy, since a low stacking fault energy is deleterious for hydrogen resistance, and in a low stacking fault energy material it is predicted that the transport efficiency is higher than in a high stacking fault energy material (Figure 30).

Also the effect of charging current supports the dislocation transport model. Increasing current density increases the amount of absorbed hydrogen. The concentration of hydrogen in a Cottrell atmosphere obeys the following equation (3).

$$C_{\perp} = C_{\infty} \exp(-E_B/kT) \quad (7)$$

where C_∞ is the matrix concentration of hydrogen and E_B the binding energy between hydrogen and dislocations. From this it follows the higher C_∞ the higher C_{\perp} (if we are below saturation level), which explains the results shown in Figure 20.

Recently, the dislocation transport theory has been supported by results of Sridhar, Kargol and Fiore [37]. Their results on Hastelloy C276 suggest that crack growth in this alloy may be governed by strain-accelerated diffusion of H to the region of maximum triaxial stress ahead of a moving crack front (Figure 31, [38]). This crack growth is discontinuous and their calculations show that this stepwise growth may arise from dislocation transport of hydrogen to this region and a build-up of a critical concentration there.

The significance of the dislocation transport mode is summarized in Table XII.

5.2 Role of Impurities in Hydrogen Permeation

In this work, thermal treatment at 650°C to produce grain boundary segregation of sulfur caused the following effects:

- thermal treatment in the S segregation range produces a galvanic difference between the grain boundary and grain interior
- for a charging current of 0.2 mA/cm^2 ($= -470\text{mV SCE}$ at which anodic processes are still thermodynamically possible) thermal treatment at 650°C produces an increase in the per-

TABLE XII
SIGNIFICANCE OF DISLOCATION TRANSPORT OF H

Effective diffusion coefficient D_{eff} is about $10^{-5} \text{ cm}^2/\text{s}$

Diffusion distance of hydrogen in 1 s is thus about 10^{-2} cm

Typical plastic zone size is about 10^{-2} cm

Distance to region of maximum triaxial stress in plastic zone ahead of crack is typically about 10^{-4} cm

Typical dislocation cell size in plastic zone is about 10^{-5} cm

Thus hydrogen can enter the metal at the tip of a crack and reach these critical distances in 1 s for a slow moving crack

meability, the increase being greater the higher the bulk S content (Figures 11-13).

for a charging current of 0.8 mA/cm^2 ($= -580\text{mV SCE}$ at which anodic processes are thermodynamically impossible) thermal treatment at 650°C does not affect permeability (Figures 11-13).

Why is there an increase in permeability at -470mV SCE but no effect at -580mV SCE ? One could consider this with the help of the Evans' diagram shown in Figure 32. The open circuit potential of a metal is a mixed potential between the reversible hydrogen potential (-310mV SCE in $0.1\text{N H}_2\text{SO}_4$) and the reversible potential of the metal (-492mV SCE for nickel). The open circuit potential of Ni in $0.1\text{N H}_2\text{SO}_4$ was -300 to -310mV SCE , i.e., about the same as the reversible potential for hydrogen evolution. This means that the reaction is under anodic control [39]. Now, when polarizing the metal cathodically above -492mV SCE , anodic dissolution can still occur. Chaung, Lumsden and Staehle [40] have shown that sulfur catalyzes anodic dissolution in Ni. In light of the above, one might think that anodic dissolution of the impurities, especially from grain boundaries which were shown to be more active, affects the hydrogen evolution reaction on the surface and enhances hydrogen entry in a manner similar to the poisoning action of these impurities when added to the electrolyte in the form of soluble compounds. At potentials more negative than -492mV SCE , the impurities segregated to the

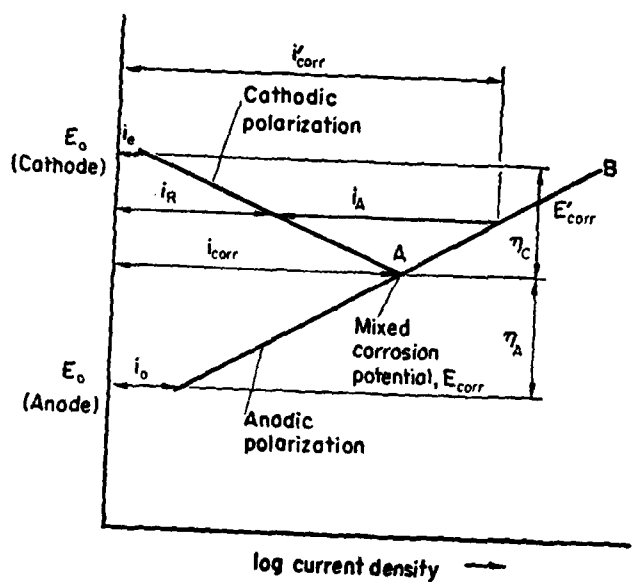


FIGURE 32. Evans' diagram [39].

grain boundaries can not dissolve and the effect of the impurities might be expected to be small since the fraction of the total surface area which is grain boundary is only 10^{-4} to 10^{-5} . This, in fact, was observed in the experiments using a charging current of 0.8 mA/cm^2 ($= -580\text{mV SCE}$).

How does sulfur increase permeability of hydrogen, either when it is dissolved from the metal or as a S containing compound added to the electrolyte. One can note that the following reaction can occur [41]



The standard potential of the reaction is -71mV SCE . Below this potential H_2S is stable. Perhaps, anodic dissolution of S from the grain boundaries might result in the formation of H_2S which is a well-known promoter [42]. When S is added in the form of sulfides, for example, the sulfides hydrolyze to form H_2S . Kawashima et al., [42] suggest that undissociated molecular H_2S enhances hydrogen absorption and permeation and thus causes an increase in hydrogen susceptibility. They suggest that H_2S acts as a bridge-forming ligand for the proton discharge step in the hydrogen evolution reaction thus accelerating the discharge reaction and entry of hydrogen.

To summarize, it was found that thermal treatment in the temperature range for S segregation increases permeability of

hydrogen at cathodic potentials when anodic dissolution is still thermodynamically possible. This was thought to be due to the dissolution of the impurities from the grain boundaries and their resulting "poisoning" action. At cathodic potentials at which no anodic processes occur the permeability is not affected by the segregation treatment.

5.3 Discussion of the Straining Electrode Experiments

Table VI shows that, at least for Ni 270, the metal is embrittled only at a cathodic potential; there is no embrittlement at the open-circuit, active, active/pассиве, and passive potentials. This result pinpoints the fact that pure nickel is embrittled by hydrogen. Indeed, the embrittlement of nickel by hydrogen is independent of the kind of electrolyte as has been demonstrated by Latanision and Opperhauser [1].

It is obvious from the result of the thermal treatment effect (Figures 23, 24, 25 and Table VII) that Ni 270, Ni 200 and Inconel 600 are not only susceptible to hydrogen embrittlement, they are also embrittled by aging around the 500°C to 700°C temperature range. It is interesting to compare the present thermal treatment result with the work done by Smialowska, Chao, Chaung and Staehle [27] in which sulphur was found to segregate at grain boundaries in Ni 200 after aging at various temperatures (Figure 3). The sulphur segregation reached a maximum at about 600°C and dropped off at 700°C and beyond. It is significant

to note that, in the present work, maximum embrittlement has been found to occur at a similar aging temperature both for Ni 270 and Ni 200 (Figures 23, 24, 25). This seems to suggest that the observed aging embrittlement is, in fact, due to the sulphur segregation at grain boundaries and that subsequent absorption of hydrogen further weakens the grain boundaries, a mechanism suggested by Yoshino and McMahon [15]. However, the fractographs have revealed that aged nickel fractures in a transgranular manner in air, and changes to an intergranular fracture morphology when the metal is exposed to hydrogen. These fracture modes are in agreement with the work done by Chaung, Lumsden and Staehle [40] in which similar straining electrode tests and heat treatments were used.* Thus, the transgranular aging embrittlement of nickel observed in the present case is unlikely to be caused by the sulphur segregation at grain boundaries. In the case of hydrogen embrittlement of nickel (lower curves in Figures 23, 24, 25) the fracture mode is intergranular. The function of the grain boundary sulphur may be visualized as enhancing hydrogen entry into the grain boundaries, and thus promoting hydrogen embrittlement, as suggested by Latanision and Opperhauser [1]. In fact, the increase in hydrogen embrittlement caused by poison addition to the electrolyte (Tables VIII and IX) supports this idea.

*In contrast, Thompson [7] has been able to fracture pure nickel intergranularly in air, and attribute it to sulphur segregation at grain boundaries, but the heat treatments he used are quite different from those used in the present work.

AD-A087 305

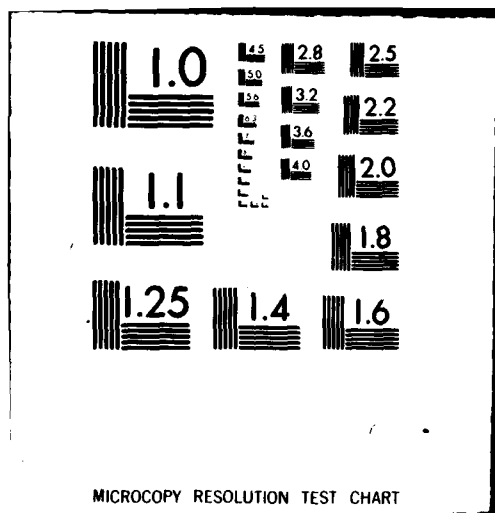
MASSACHUSETTS INST OF TECH CAMBRIDGE CORROSION LAB F/6 11/6
HYDROGEN INDUCED INTERGRANULAR CRACKING OF NICKEL-BASE ALLOYS. (U)
JUL 80 M KURKELA, T S LEE, R M LATANISION N0001N-78-C-0002
NL

UNCLASSIFIED

TR-4

2 x 2
 $\frac{1}{2} \times \frac{1}{2}$

END
DATE
FILED
9-80
DTIC



An alternative explanation is that, if a critical hydrogen concentration at grain boundaries is necessary to cause hydrogen embrittlement, then the function of the grain boundary sulphur is to reduce this critical concentration and enhance embrittlement.

The cause of aging embrittlement for the more complicated Inconel 600 alloy system is not clear, but it is interesting to observe the results obtained by Latanision, Pelloux, Was and Ballinger [43] that when Inconel 600 is aged at 700°C, chromium carbide precipitates at grain boundaries and there is a Cr-depletion zone in the vicinity of the grain boundary.

Looking at the thermal treatment results for Ni 270 and Ni 200 one can see that for the purer Ni 270, hydrogen embrittlement is far more significant than aging embrittlement (Figure 25), whereas in the less pure Ni 200, aging embrittlement becomes more profound and the effect of hydrogen embrittlement is reduced (Figure 23). This raises the possibility that impurities in Ni 200 may, on one hand, embrittle the metal, and on the other hand, suppress the effect of hydrogen as an embrittling species. Although the mechanism is not exactly known, it is not unreasonable to presume that impurities in the metal matrix (such as carbide particles) act as traps for hydrogen, so that the amount of hydrogen available to the grain boundaries is decreased.

One important feature of the straining-electrode experiment is that, given a short testing period of about one or two hours and without the benefit of precharging hydrogen into the metal,

hydrogen can severely embrittle the material. If diffusion of hydrogen through the metal lattice to some defect sites is a prerequisite for hydrogen embrittlement, then this experiment must suggest some kind of fast hydrogen transport mechanism, rather than just the lattice diffusion in order to realize the embrittlement. It is believed that dislocation transport is the major mechanism to carry hydrogen when the material is being plastically deformed [3], as has been demonstrated by the permeation experiments with specimens undergoing plastic deformation. Table X shows that the effect of hydrogen is reduced by increase in strain rate. The permeation experiments have shown that at higher strain rates, hydrogen permeates the metal faster than at lower strain rates (Figure 18). At a higher strain rate, hydrogen would be transported faster to grain boundaries by dislocations, but it would also be swept away faster from grain boundaries by dislocations. The net result being that there is less hydrogen retained at the grain boundaries. If this is true, it should then be expected that an increase in strain rate reduces the susceptibility to intergranular hydrogen cracking, even though it increases the hydrogen permeation through the metal. Actually this strain rate effect has been reported in the literature [44].

In principle, there is a critical dislocation velocity above which the mobile dislocations would out-run their hydrogen atmospheres such that the dislocations would become ineffective

in transporting hydrogen. This implies that there should exist a critical strain rate above which no hydrogen embrittlement would occur, if dislocation transport is necessary for the embrittlement. So it is interesting to run the straining electrode experiments in the future to cover a wider range of strain rates and to discover the critical strain rate.

Comparing the results shown in Figures 23 and 24, one can see that finer-grained Ni 200 is less susceptible to embrittlement caused by hydrogen or by aging than the coarser-grained material. That nickel with smaller grain size is less susceptible to hydrogen embrittlement is a well-known phenomenon. This reduction in susceptibility can be explained by (a) the reduction of segregation of impurities at grain boundaries due to the increase in grain-boundary area per unit volume, (b) the decrease in the efficiency of dislocation transport by shortening the dislocation mean-free-path, and (c) the reduction of hydrogen build-up at the grain boundaries for a given dislocation transport rate, due to the larger grain boundary area available to take up the transported hydrogen.

5.4 The Effect of Promoters on Permeation of Hydrogen

The effect of promoters additions on both permeation and cathodic polarization in our experiments was similar to the results obtained for iron-base alloys [45].

Group V-A and Group VI-A elements affect cathodic behavior differently. S and Se (VI-A) were found to accelerate the overall cathodic kinetics, whereas, As and Sb decreased the cathodic kinetics but increased the hydrogen overvoltage (Figure 29). The hydrogen evolution reaction consists of several steps and the two promoter groups could affect different steps but the end result in both cases is increased absorption of hydrogen.

It is often said that the promoter elements enhance hydrogen entry into the metal because of their low exchange current densities, $i_{O,H}$ (Figure 33). Thus, their presence on the surface would shift the cathodic kinetics to the left in Figure 33. As and Sb were found to act this way, but not S and Se. (Figure 29).

When one compares the effect of promoters in the absence and presence of plastic deformation, one notices that their role is not as significant when the metal is undergoing plastic deformation. This agrees with the findings of Smialowski [46] on steels. He found that in a 0.56% C steel embrittlement increased only slightly in dynamic testing due to the addition of As and Se. On the other hand, in static experiments there was a significant effect. A possible explanation [45] is that in the presence of plastic deformation new slip steps form continuously on the metal surface and "fresh" surface is exposed continuously. The formation of slip steps is possibly faster than the adsorption of promoters. So, the adsorption and absorption of hydrogen would take place largely on fresh uncontaminated surfaces without the catalytic effect of the promoters.

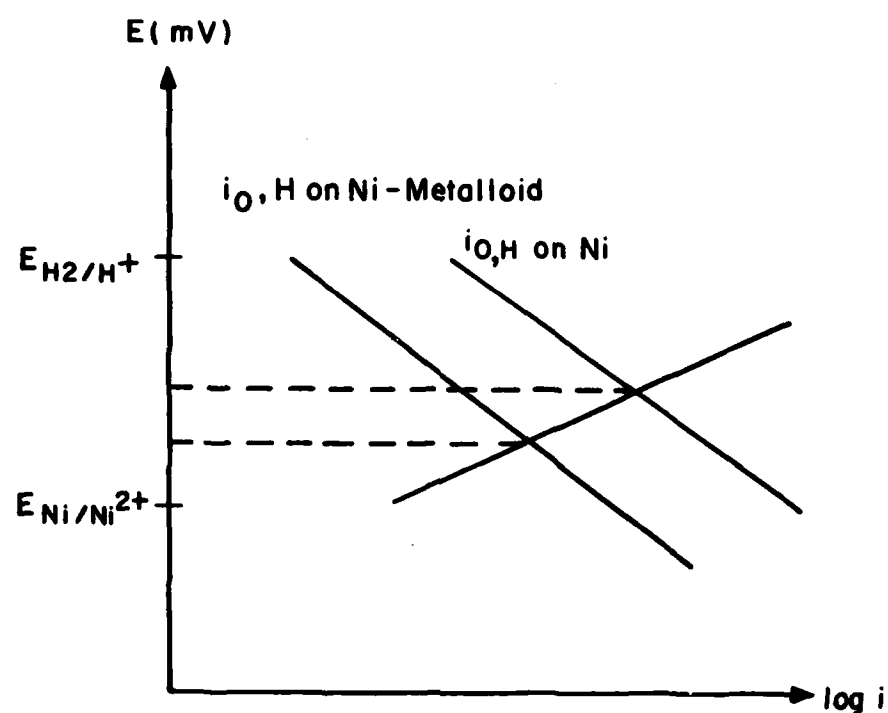


FIGURE 33. Diagram showing schematically the effect of promoter elements on hydrogen evolution kinetics.

5.5 Diffusion Kinetics Considerations

The hydrogen diffusivity measurements indicated the following:

- the grain size does not have any significant effect on diffusivity which seems to indicate that grain boundary diffusion is probably not a dominant diffusion mechanism
- the diffusion coefficient D_H decreases when the alloying and impurity content increases, i.e., $D_{\text{Marz Ni}} > D_{\text{Ni 270}} > D_{\text{Ni 200}}$

The values of the diffusion coefficients were in good agreement with data of Robertson [47] who did gas phase permeation studies. The diffusion coefficients are the same as the values in single crystals so that diffusion probably occurs by lattice diffusion mechanism. If grain boundary diffusion were significant, one would expect D to increase with decreasing grain size. In agreement with Robertson [47], no such effect was observed. On the other hand, the permeation technique might not be sensitive enough because the total grain boundary area is very small compared with the total grain interior area.

The lowering of the diffusion coefficient with increase in impurity content is likely due to trapping of hydrogen by the solute impurities [48].

6. CONCLUSIONS

The results of the strained electrode and permeation experiments lead us to suggest that the hydrogen induced intergranular cracking in nickel could be interpreted in terms of a "critical grain boundary hydrogen concentration model." This is to say that intergranular cracking may result when a critical concentration of hydrogen is achieved there. This can explain the effect of grain size and promoter additions to the electrolyte. In a large grain size material there is less grain boundary area per unit volume and thus we attain the critical grain boundary concentration more quickly. In the presence of poisons in the electrolyte, the amount of hydrogen absorbed increases and thus we attain the critical grain boundary concentration more quickly. The role of grain boundary segregation might then be to reduce this critical hydrogen concentration at grain boundary required for cracking. The impurities seem to stimulate hydrogen entry only when anodic dissolution of the impurities can occur (mainly from the grain boundaries where they can be enriched to concentrations up to 10000 times the matrix concentration). To reduce embrittlement one would thus have to prevent or reduce the build-up of a critical concentration of H at grain boundary by having other trapping sites available in the microstructure. We think that hydrogen embrittlement is less serious in Ni 200 (as compared with

Ni 270) because there are more traps in the matrix (due to a higher solute content) which, in turn, make less hydrogen "available" for the grain boundaries. As far as hydrogen transport is concerned, transport in the form of Cottrell atmospheres along with mobile dislocations seems to dominate. No evidence of short circuit grain boundary diffusion was found. Dislocation transport seems to be of great significance in the embrittlement of polycrystalline nickel.

ACKNOWLEDGMENTS

It is a pleasure to thank our colleagues Rob Sorensen, Gary Was, Ron Ballinger, and Hermann Tischner for many useful comments during the course of this work. Likewise, the support and encouragement of Dr. P.A. Clarkin of the Office of Naval Research is gratefully acknowledged.

REFERENCES

1. R.M. Latanision and H. Opperhauser, Jr., Met. Trans. 5, p. 483 (1974).
2. R.M. Latanision and H. Opperhauser, Jr., Proc. 3rd Int'l Conf. on Strength of Metals and Alloys, Institute of Metals, 1, p. 472 (1973).
3. J.K. Tien, A.W. Thompson, I.M. Bernstein and R.J. Richards, Met. Trans., 7A, p. 821 (1976).
4. B.J. Berkowitz and R.D. Kane, Corrosion, 36, p. 24 (1980).
5. R.D. Kane and B.J. Berkowitz, Corrosion, 36, p. 29 (1980).
6. J.D. Frandsen, H.L. Marcus and A.S. Tetelman, Effect of Hydrogen on Behavior of Materials, The Metallurgical Society of AIME, New York, p. 299 (1976).
7. A.W. Thompson, Grain Boundaries in Engineering Materials, Claitor's, Baton Rouge (1975).
8. H.L. Marcus and P.W. Palmberg, Trans. TMS-AIME, 245, p. 1664 (1969).
9. D.F. Stein, A. Joshi and R.P. Laforce, Trans. ASM, 62, p. 766 (1969).
10. R.M. Latanision, O.H. Gistine and C.R. Compeau, in Environment Sensitive Fracture of Engineering Materials, p. 48, TMS-AIME, 1979.
11. T.R. Pinchback and L.A. Heldt, in Environment Sensitive Fracture of Engineering Materials, p. 250, TMS-AIME, 1979.
12. J.H. Westbrook, "Stress Corrosion Cracking and Hydrogen Embrittlement of Iron Base Alloys," NACE Houston, p. 26 (1977).
13. J.P. Hirth and H.H. Johnson, Corrosion, 32, p. 3 (1976).
14. R.L. Cowan II and G.M. Gordon, "Stress Corrosion Cracking and Hydrogen Embrittlement of Iron Base Alloys," NACE, Houston, p. 1023 (1977).
15. K. Yoshino and C.J. McMahon, Jr., Met. Trans., 5, p. 363 (1970).
16. P. Bastien and P. Azou, C.R. Acad. Sci. Paris, 232, p. 1845 (1951).

17. P. Bastien and P. Azou, 1st World Metallurgical Congress, ASM, Cleveland, p. 535 (1951).
18. B.A. Wilcox and G.C. Smith, Acta Met., 13, p. 331 (1965).
19. A.H. Windle and G.C. Smith, Met. Sci. Jour., 4, p. 136 (1970).
20. G.C. Smith, Hydrogen in Metals, I.M. Bernstein and A.W. Thompson, eds., ASM, Metals Park, (1974).
21. R.M. Latanision and R.W. Staehle, Scripta Met., 2, p. 667 (1968).
22. M.R. Louthan, G.R. Caskey, J.A. Donovan and D.E. Rawl, Mat. Sci. Eng., 10, p. 357 (1972).
23. J.A. Donovan, Met. Trans., 7A, p. 145 (1976).
24. L.M. Foster, T.H. Jack and W.W. Hill, Met. Trans., 1, p. 3117 (1970).
25. H.H. Johnson and J.P. Hirth, Met. Trans., 7A, p. 1543 (1976).
26. A.J. West and M.R. Louthan, Jr., Met. Trans., 10A, 1675 (1979).
27. S. Smialowska, C.Y. Chao, H.E. Chaung and R.W. Staehle, Journal of Electrochem. Soc., 126, p. 2038 (1979).
28. S. Floreen and J.H. Westbrook, Acta Met., 17, p. 1175 (1969).
29. M.A. Devanathan and Z. Stachurski, Proc. Roy. Soc., 270A, p. 90 (1962).
30. A.J. Kunnick and H.H. Johnson, Met. Trans., 5, p. 1199 (1974).
31. J. McBreen, L. Nanis and W. Beck, J. Electrochem. Soc., 113, p. 1218 (1966).
32. T.K. Govindan Namboodhiri and L. Nanis, Acta Met., 21, p. 663 (1973).
33. N. Boes and H. Zuchner, J. of Less-Common Metals, 49, p. 223 (1976).
34. J.G. Early, Acta Met., 26, p. 1215 (1978).
35. N.D. Greene, "Experimental Electrode Kinetics, Rensselaer Polytechnic Institute, Troy, New York (1965).

36. J.O'M. Bockris and A.K.N. Reddy, Modern Electrochemistry, Plenum Press, p. 1238 (1973).
37. N. Sridhar, J.A. Kargol and N.F. Fiore, Scripta Met., 14, p. 225 (1980).
38. J.R. Rice, "Stress Corrosion Cracking and Hydrogen Embrittlement of Iron Base Alloys," NACE, Houston, p. 11 (1977).
39. J.C. Scully, The Fundamentals of Corrosion, 2nd ed., Pergamon Press, Oxford (1975).
40. H. Chaung, J.B. Lumsden and R.W. Staehle, Met. Trans., 10A, p. 1853 (1979).
41. M. Pourbaix, Atlas of Electrochemical Equilibria in Aqueous Solutions, Pergamon Press, Oxford, p. 549 (1966).
42. A. Kawashima, K. Hashimoto and S. Shimodaira, Corrosion, 32, p. 321 (1976).
43. R.M. Latanision, R.M. Pelloux, G.S. Was and R.G. Ballinger, Third Semi-Annual Progress Report for EPRI, January 1980.
44. A.H. Windle and G.C. Smith, Met. Sci. J., 4, p. 136 (1970).
45. R.D. McCright, "Stress Corrosion Cracking and Hydrogen Embrittlement of Iron Base Alloys," NACE, Houston, p. 316 (1977).
46. M. Smialowski, Congres International L'Hydrogene dans les Metaux, Editions Science, Paris, p. 300 (1972).
47. W.D. Robertson, Z. Metallkunde, 64, p. 436 (1973).
48. R.A. Oriani, Acta Met., 18, p. 147 (1970).

1. *Leucostethus* *leucostethus* (Linné)

2. *Leucostethus* *leucostethus* (Linné)